NASA Contractor Report 191118

Internal Strain Analysis of Ceramics Using Scanning Laser Acoustic Microscopy

Renee M. Kent
University of Dayton
Dayton, Ohio

March 1993

Prepared for
Lewis Research Center
Under Cooperative Agreement NCC3–81

NASA
National Aeronautics and
Space Administration

Multiple Pages Intentionally Left Blank

TABLE OF CONTENTS

LIST OF TABLES

LIST OF FIGURES

LIST OF SYMBOLS AND ABBREVIATIONS

α	coefficient of thermal expansion
α-	material consisting of alpha phase (HCP)
β-	material consisting of beta phase (cubic)
γ	surface free energy
Γ	amplitude of surface corrugation of ultrasonic wave
δ	acousto-optical path difference
ϵ	engineering strain
ϵ_r	relaxation strain induced by external stress
θ	angle of insonification
λ	optical wavelength in vacuum
Λ	acoustic (ultrasonic) wavelength in a medium
ν_{ij}	Poisson's ratio
N	frequency of acoustic (ultrasonic) wave
ξ	strain modulation coefficient
ρ	mass density

σ	engineering stress
τ	frictional stress between the matrix and fiber
τ_0	time shift in cross correlation velocity measurement
ϕ	diameter of reinforcing fiber
χ	constant characteristic of crack geometry
ψ	phase
ω_m	modulation frequency due to acousto-optics
Al_2O_3	aluminum oxide, alumina, sapphire
ASTM	American Society of Testing and Materials
b	width of MOR bar (in this work, 4 mm)
B_{ij}	relative dielectric impermeability tensor
c	crack length
CAS	calcium alumino-silicate glass ceramic
CMC	ceramic matrix composite
d	thickness of MOR bar (in this work, 3 mm)
D	diameter of aperture in optical imaging system
E	elastic modulus
f	focal length of focusing lens in imaging system
f/*	f-number of optical imaging system
FRC	fiber reinforced composite

HeNe	helium neon gas discharge laser (λ = 6328 nm)
I	moment of inertia
K_c	critical stress intensity
l	specimen gauge length
LAS	lithium alumino-silicate glass ceramic
MOR	modulus of rupture
n_0	index of refraction in test medium
p_{ij}	strain optic coefficient
R	Rayleigh resolution
ROI	region of interest; measurement location on a test specimen
SiC	silicon carbide
SLAM	scanning laser acoustic microscope
SNR	signal to noise ratio
v	velocity of acoustic wave propagation in a test medium
V_i	volume percent of *i* in total composite

Renee M. Kent*
University of Dayton
Dayton, Ohio 45469

CHAPTER I

INTRODUCTION

Ceramics and ceramic composites are brittle materials which require nonintrusive testing and evaluation. Ceramics exhibit desirable properties such as high specific strengths, high elastic modulus, structural integrity at elevated temperatures, and in many cases, resistance to thermal shock and oxidation that make them viable candidates for high temperature structural applications. However, most ceramics have a characteristically low fracture toughness. Any flaws, either inherent in the material or externally caused, act as stress concentrators and become the sites for crack initiation [1]. In brittle materials, there is little impedance to crack propagation and catastrophic failure occurs.

A quantitative verifiable data base for advanced ceramic materials is necessary to properly select materials for specific applications. Nonintrusive measurement methodologies are integral for the analysis of ceramic materials since deleterious contact with the specimen must be avoided during the measurement process. Such contact can cause damage which destroys the structural integrity and/or alters the

*NASA Resident Research Associate at Lewis Research Center.

material behavior response, rendering the measurements invalid. Nonintrusive methods eliminate these issues.

Historical Background

Fiber reinforced composite (FRC) structures occur naturally in living organisms. As an example, the human bone is a fiber reinforced composite structure consisting of stiff collagen fibers in a hydroxyapatite matrix [2]. The fibers are oriented to resist the principal loads and the microstructure can be reoriented to respond to changes in system loading, thus providing a remarkably tough structure with high load bearing capacity. Similarly, wood is a fiber reinforced composite with fibers of crystalline cellulose microfibrils and a matrix consisting of lignin and hemicellulose [3]. The wings of beetles and reptiles such as the pterosaur (now extinct) have also been shown to be composite structures [4].

Man-made fiber reinforced composites were established centuries ago. The Processional Way in ancient Babylon was constructed of bitumen reinforced with plaited straw. At least as far back as the 1700s, the British used pulp wood or horse hair fibers to reinforce plaster ornaments and mud bricks. In the United States, the use of cellulose fiber reinforced plasters and cements were introduced in the late 18th century [3].

However, it was not until the discovery of boron and graphite fibers in the early 1960s that FRCs became serious contenders for high performance structural applications. With the aim to provide more lightweight components, the United States, through federally funded programs, led the way for the development of composites to replace metals in secondary structures in airframes [5,6,7]. By the end of the decade, the industry had progressed to replace primary aircraft components with graphite-epoxy and boron-aluminum composites for their military aircraft. The F-14, F-15, F-16, F/A-18, and AV8-B each contain 3-20 percent composites by weight [8,9].

Throughout the following decade, as the composites used for aerospace technology were adapted for commercial applications [10], the technological goals within the aerospace industries continued to drive the evolution of composite processing and systems design. At the same time, the process for manufacturing glass ceramic matrices as first demonstrated in a rudimentary fashion by Reaumur, a French chemist, was refined by Corning Glass Works to produce high strength glass ceramics. In Reaumur's early work, glass bottles were packed in a mixture of sand and gypsum and subjected to red heat to convert the glass to opaque porcelain [11]. Though Reaumur's process lacked sufficient control of the crystallization process to produce high strength glass ceramics, approximately 200 years later, S.D. Stookey of Corning discovered that the addition of small metallic particles to the glass

composition provided sites for nucleation for the crystallization of the major phase of the glass and promoted controlled crystallization under appropriate heat treatment. These materials offered matrices sufficient to sustain elevated temperature operation for FRC applications.

Though existing composites were restricted to applications that experienced a maximum use temperature of 300°C, the increased demand for more fuel efficient aircraft that could sustain higher payloads spawned the development of glass ceramic matrix composites reinforced with graphite or alumina fibers [12]. These materials exhibit high strength and fracture toughness at temperatures to 1000°C [13]. Development of high strength silicon carbide (SiC) fiber monofilaments for reinforcement of glass ceramic matrices provided composites having operating temperature capabilities to 1300°C.

As we approach the late 20th and early 21st centuries, modern aerospace vehicles are being designed to operate under exceedingly adverse conditions. Vehicles such as the high speed civil transport (HSCT) [14], the National Aerospace Plane (NASP) [15,16,17] which is expected to operate in excess of Mach 5, and the Advanced Tactical Fighter (ATF) [16,18] will generate temperatures in the combustor and nozzle assemblies to 1650°C (3000°F). These conditions and the desire to improve system performance (thrust to weight ratio) prompt the need for innovative lightweight materials which maintain their structural integrity at temperatures to

1650°C (3000°F) [19]. While ceramic materials have properties which make them viable for such applications, non-metallic materials have traditionally been avoided for such critical structural engineering applications due to their low fracture toughness. Therefore, recent efforts have focused upon engineering the ceramic microstructure to develop ceramic matrix composites (CMC) with improved fracture toughness for elevated temperature structural applications [20].

Some glass ceramic matrix composites reinforced with silicon carbide fibers are being studied for elevated temperature applications [21]. However, silica based nonoxides such as silicon carbides and silicon nitrides, and alumina based oxides are currently the primary candidates for the critical components since current elevated temperature materials exhibit strength degradation and creep at temperatures above 1300°C [22].

Effective process development of ceramic composite structures demanded nonintrusive analysis of the internal structure of the materials. Such analysis of ceramic and ceramic composite materials was advanced by implementation of acoustic microscopic techniques which permitted the nonintrusive interrogation of the internal structure of opaque materials. Acoustic microcopy was first proposed in 1936 by Sokolov [23] though technological limitations of the time obstructed practical development of the device. In 1956, Dunn and Fry [24] conducted the first acoustic microscopy experiments. However, it was not until the late 1960s and early 1970s

that practical acoustic microscopes were developed. During this era, the scanning acoustic microscope (SAM) which used a confocal arrangement of acoustic lenses to investigate specific regions of opaque test specimens was developed by Quate et al. [25]. An alternate methodology which used a scanning laser beam for detection of an ultrasonic wave propagating through a test specimen was developed by Korpel et al. [26]. This latter technology, the scanning laser acoustic microscope (SLAM) demonstrated enhanced capabilities for analysis of ceramic materials. These capabilities will be described in more detail later in this and the following chapters.

Statement of the Problem

Accurate quantitative characterization of the ceramic matrices and fibers reinforcing ceramic composite structures is essential for the reliable evaluation of composite structures under expected operating conditions. However, there is presently no definitive technology for the reliable strain analysis of small diameter ceramic fibers.

Ceramic fibers, typically on the order of tens of microns in diameter, require high resolution methodologies for measurement of their mechanical behavior properties. The ASTM standard test method for measurement of single filament materials [27] suffers from lack of long term repeatability and accuracy [28].

Accurate analysis of the ceramic monolithic and FRC structures requires an investigation of the mechanical behavior properties at the microstructural level. The

probability of failure of an FRC is related to the statistical flaw population and the influence of external factors (e.g. stress, temperature) on the orientation and distribution of the flaw population. The material's microstructure plays a significant factor in determining the mechanical behavior properties of the material by contributing to the net crack driving force at the local level [29]. However, few experimental test devices provide reliable quantitative data of mechanical properties as related to microstructure.

Purpose of the Investigation

The primary objective of this research is to develop and demonstrate a technique to nonintrusively measure the in situ tensile strains developed in small diameter ceramic fibers and the local strains induced in ceramic and ceramic composite systems by an externally applied flexural load. These strains can then be used to determine the internal stresses caused by cumulative damage within the material and related to the microstructural development of the material. To develop a thorough understanding of the composite, the research program includes the analysis of each phase of the composite as well as the composite system.

The primary methodology for the local strain analysis conducted in this study is based on the scanning laser acoustic microscope (SLAM), first developed for qualitative internal structural analysis of opaque materials [26,30]. The SLAM is a

nonintrusive instrument with which reliable quantitative analyses of brittle materials can be achieved.

In the SLAM, the propagation of the acoustic wave through a material (test specimen) provides the capability of monitoring the internal structure. Acousto-optical coupling used for detection provides the high resolution capability necessary for ceramic fiber monofilament studies and the localized nonintrusive probing necessary for FRC analysis. In this work, the SLAM system was improved to allow the direct monitoring and analysis of the acousto-optical response of the SLAM, as a test specimen was stressed, to generate an in situ analysis of the material.

There are several pertinent points which must be considered in order for the SLAM to successfully provide strain measurements of small diameter ceramic fibers and FRCs. These include:

1. The small diameter and brittle nature of fibers make it difficult to apply uniaxial tensile loads to the fiber. A practical method for specimen loading must be devised which allows optical probing of the fiber but concurrently minimizes frictional effects and off-axis bending as the fiber is loaded.
2. The ultrasonic wave propagation of the SLAM requires that an acoustic couplant be used. For room temperature analyses, water provides a convenient couplant. However, this limits the configurations which may be used for appropriate uniaxial tensile loading of the fiber test specimen and/or

four-point flexural loading of FRCs.

3. Accurate measurements require a calibration standard. However, acoustic standards are not yet available due to difficulties in obtaining reproducible responses from a given material set. Most materials contain subtle microstructural differences from specimen to specimen which affect the reliability of the acoustic standard. The measurement method employed must take such considerations into account.

4. The SLAM parameters must be chosen such that the resolution is adequate to perform the required analysis and the signal to noise (SNR) is not degraded due to attenuation of the signal. However, there is an inherent tradeoff between resolution and attenuation. Highly attenuating materials, such as FRCs, may require lower resolution measurements.

5. A methodology for analyzing the optical response from the material test specimen in a quantitative manner must be provided.

The following chapters of this dissertation will focus on a detailed discussion of these features as it applies to the theoretical and experimental implementation of nonintrusive strain analyses.

CHAPTER II

THEORY

The limited number of slip systems and large Burger's vectors of monolithic ceramics promote catastrophic failure once cracks have initiated. Polycrystalline ceramics fail in a brittle manner largely because there is little to impede the accelerating crack once it has initiated. However, efforts have been made to improve the fracture toughness of ceramics while still maintaining the desirable material properties [31]. Brittle matrix composites appear to offer a means for improving the fracture toughness. In ceramic composites, reinforcing fibers of high strength and elastic modulus are placed in the ceramic matrix. Ideally, these reinforcing fibers retain their high theoretical strengths due to the presence of statistically insignificant flaw populations; the smaller the fiber the lower the flaw probability. The composite material is strengthened by effective load transfer to the reinforcing fibers, and toughened by crack blunting and crack deceleration at the matrix-fiber interface.

Mechanics of Composites

The reinforcing fibers positioned in the composite strengthen and toughen the specimen by two primary mechanisms. When a tensile load is applied to the reinforced material along the direction of the fiber, some of the applied load is transferred from the weaker matrix to the stronger fiber reinforcement. To a first approximation, this load transfer is described by the rule of mixtures [32]. An analogous relation is used to describe the effect of the elastic modulus of the composite material. The rule of mixtures model approximation assumes that there are no voids in the material and that the fibers are unidirectional and the same length as the matrix. It has been shown, in previous work, that this rule of mixtures approximation is quite accurate for the lithium alumino-silicate (LAS)/Nicalon β-SiC fiber composite system which was used in this study [33].

The reinforcing fiber toughens the material by introducing an impedance to the accelerating crack as it propagates. During processing, a weak bond is formed between each individual fiber and the surrounding matrix. Since the individual fibers are nearly defect-free, any sites for crack initiation are likely to be in the matrix. When stress is applied to the material, the stress is concentrated at the matrix flaws and cracks begin to propagate. However, when the crack reaches the fiber, its path is deviated to follow the path of least resistance: along the length of the fiber. This abrupt change in propagation direction takes energy and the crack is slowed. In

addition, the crack is forced in a direction parallel to the direction of the applied load and the stresses in this direction tend to close the crack due to the Poisson effect. This is illustrated in Figure 1.

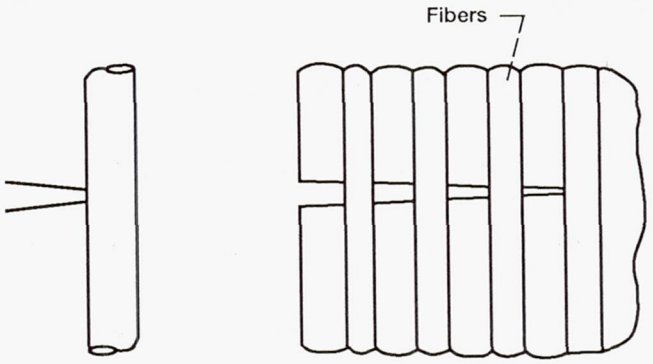

Figure 1.—Crack blunting in a composite.

Ideally, a weak bond is formed at the interface between the matrix and the fiber. This is a critical parameter in the design and study of composite structures. As the composite material is stressed along the fiber axis, the fibers slide along the matrix. If the bond is weak enough, the primary resistance to fiber slippage is the frictional force between the fiber and the matrix. These frictional stresses also effect the nature of microcracking during loading. In an ideally linear elastic monolithic ceramic, the crack tends to open and propagate during loading and close during unloading. The fibers tend to oppose each of these conditions. Crack extension is inhibited by frictional forces during the initial loading of the material but crack closure is opposed during specimen unloading. These characteristics of FRCs must

be taken into account when characterizing the internal stresses which develop as damage accumulates in the matrix.

In general, the linear elastic fracture mechanics (LEFM) analysis approach is not applicable for composites. The fundamental underlying assumption of LEFM is that the material behaves ideally elastically, i.e., according to Hooke's Law where the constant of proportionality between stress and strain is the elastic modulus of the material. However, the absorption of crack propagation energy which occurs in ceramic composites forces the material to behave nonlinearly. This has been experimentally demonstrated in LAS/SiC fiber reinforced materials [34,35]. In addition, LEFM is not applicable because unidirectional fiber reinforced composites are anisotropic. In that case, the relationship between stress and strain is most generally described by

$$\sigma_i = C_{ij}\epsilon_j \qquad (1)$$

where σ is the stress tensor, ϵ is the strain tensor, and C is the three-dimensional stiffness tensor. For orthotropic materials, such as the unidirectional composites used in this study, the stiffness is uniquely described with nine independent constants [36,37].

Effects of Residual Stresses

Internal residual stresses often develop during processing of both ceramic monolithics and composites. Residual stresses in monolithics develop primarily from anisotropy of material properties along orthogonal crystallographic directions. This causes anisotropic expansion of the material during heat treatment. In addition, temperature gradients within the material augment the development of internal stresses. Residual stresses can also develop from unrelaxed volume changes resulting from phase transformations which occur when the crystalline glass ceramic is formed from the glass composition.

The LAS monolithic system studied in this work develops large residual stresses during processing due to its highly anisotropic coefficients of thermal expansion [38]. The system retains large amounts of potential energy and fundamentally occupies an energetically unfavorable state. This can lead to the development of microcracks or flaws which relieve the internal stress in the processed LAS material.

Most current composites have a coefficient of thermal expansion mismatch between the matrix and the fiber. During processing, the difference in thermal expansion coefficients leads to the generation of residual stresses in both the matrix and the reinforcing fiber. In the LAS/SiC fiber composites used in this study, there is a very large coefficient of thermal expansion mismatch,

$$\Delta\alpha = \alpha_f - \alpha_{LAS} = 4.3\times10^{-6} \quad (2)$$

Hence, there are large residual tensile stresses developed in the fiber and residual compressive stresses in the LAS matrix during processing. In the case of calcium alumino-silicate (CAS)/SiC composites,

$$\Delta\alpha = \alpha_f - \alpha_{CAS} = -1\times10^{-6} \quad (3)$$

There are residual tensile stresses in the matrix due to processing.

Residual stresses alter the observed mechanical behavior of the material. These residual stresses transform the nature of the failure mechanisms typically observed in the LAS/SiC fiber composites [39,40]. It has been shown that tensile failure of unidirectional LAS/Nicalon composites is precipitated by matrix cracking while failure in four-point flexure involves buckling on the compressive side of the bar [39,41]. This implies that the composites are stronger in tension than compression. However, Marshall and Evans point out that after the microcracks have dominated the tensile surface of the specimen, the matrix has little effect on the subsequent stress distribution and the flexure beam is no longer linearly elastic. Examination of the flexure fracture surfaces shows that matrix cracking which initiates on the tensile side of the flexure bar stops at midplane. These observations suggest that the flexural strength data cannot be used to predict tensile behavior but can be used to predict the onset of matrix cracking.

Ceramic Matrix Cracking

The stress at which the first matrix damage occurs is likely to be the damage tolerance design criteria for composite systems. Matrix cracks indicate the onset of permanent damage in the system and the occurrence of nonlinear behavior. It has been shown that composite failure strains can significantly exceed those of matrix cracking if the fiber strengths are high. However, microcracking in the matrix permits the ambient atmosphere to permeate the composite. This causes degradation of the composites at elevated temperature (up to 1000°C) in LAS/SiC composites due to internal oxidation [42].

The stress required to initiate and propagate matrix cracks has been calculated by Aveston et al. [43] using an energy balance analysis and independently by Marshall et al. [44] using a fracture mechanics approach. These models are described in Appendix A.

Experimental evidence to support the matrix cracking models has assumed that the stress at which the onset of matrix cracking occurs and the initiation of nonlinear mechanical behavior are coincident [39]. However, recently researchers have reported experimental evidence which shows that the first matrix cracking stress in FRCs actually occurs prior to the onset of nonlinearity. Using the method of acoustic emission to experimentally detect the first matrix cracking stress, similar

results have been obtained for fiber reinforced SiC/RBSN (reaction-bonded silicon nitride) [45] and independently for CAS/SiC and LAS/SiC [46,47].

Nonintrusive Testing of Ceramics

The scanning laser acoustic microscope (SLAM) is a nonintrusive technique for evaluating the internal structure of a material [48,49,50]. The SLAM is shown schematically in Figure 2. A piezo-electric transducer generates a high frequency acoustic (ultrasonic) wave which propagates through the material. The phase front of the acoustic wave is altered as the wave is reflected and/or scattered from elastic inhomogeneities in the specimen. These acoustic perturbations within the material structure are detected by the scanning laser beam to reveal variations in the internal structure of the material. At the detector plane, the optical signal is superposed with an electronic phase signal to produce interference fringes characteristic of the internal material structure. A more detailed analytical description of the SLAM operation is found in Appendix B.

The SLAM system offers unique capabilities compared with other conventional acoustic techniques due to the use of the scanning laser detection system. Acoustical techniques provide advantages for the characterization of materials which are optically opaque by allowing the internal material structure to be nondestructively monitored. Unfortunately, the resolution of many acoustic testing systems is limited

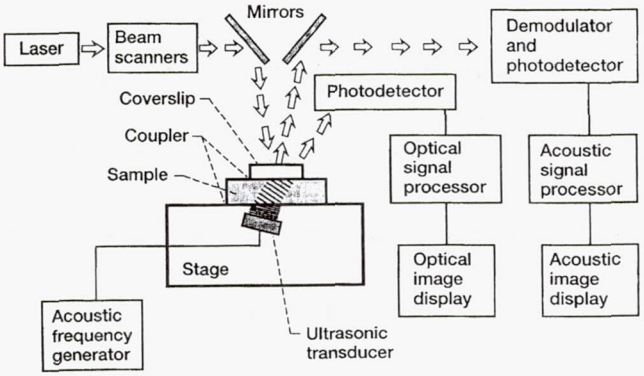

Figure 2.—Schematic of scanning laser acoustic microscope.

by the efficiency of the detection. Acoustic to acoustic coupling affords comparatively low detection efficiency and larger area detector crystals are used to improve the signal strength. However, the system resolution is degraded as the detector surface area is increased. In the scanning acoustic microscope (SAM), for example, the resolution is limited to the acoustic focal spot size in the material (~400 μm in ceramics) [51]. By comparison, the resolution of the SLAM is diffraction-limited since optical coupling is used for detection. Using the Rayleigh criteria for resolution, the resolution of the SLAM is

$$R = 1.22 \Lambda f/* \qquad (4)$$

where Λ is the acoustic wavelength, and $f/*$ is the f-number of the detection system. The acoustic wavelength is related to the velocity of sound through the material being

studied and the frequency of the ultrasound. In terms of frequency,

$$R = 1.22 \frac{v}{N} f/* \qquad (5)$$

where v is the velocity of the ultrasound through the material and N is the frequency of the ultrasound. The attainable system resolution is material dependent but, in general, increases with increasing frequency. In most of the studies considered in this work, the operating frequency used in the SLAM was 100 ± 4 MHz. At this frequency, the attainable diffraction-limited resolution in typical ceramics is 15-25 μm.

The SLAM has, to date, been used primarily for internal defect detection and characterization in ceramics and other materials [52-56]. Little has been done to quantitatively characterize the state of the material. However, by directly analyzing the SLAM optical signal response, it is possible to develop a quantitative capability of the system for the measurement of internal strains introduced in ceramics and composite systems by externally applied loads. A model relating strain to measurable SLAM parameters is detailed in Appendix C.

CHAPTER III

EXPERIMENTAL STUDIES

The primary objectives of this research were to develop a nonintrusive strain measurement capability for ceramics, and to implement the technique for the strain analysis of small diameter ceramic fibers in tension and the local in situ strain measurements of ceramic matrices and composites in four-point flexure. These strains can then be used to determine the internal stresses caused by cumulative damage within the ceramic materials. To develop a thorough understanding of the composite system, the research program included the analysis of each phase of the composite as well as the total composite system.

The fundamental instrumentation used for this study was based on the scanning laser acoustic microscopy (SLAM) technology originally developed in the late 1960s for characterizing the internal structure of optically opaque materials. In this work, the SLAM technology was extended to allow a more quantitative measure of the material properties. It was not the intent of this research to inspect for debonding or other flaws per se, although in practical application of the techniques

used in this research, defect inspection may be performed concurrently. Some examples of this feature are also provided in this work.

Since the SLAM is a laser scanning system, the planarity and surface roughness of the specimens were critical parameters. A rough surface contour would produce undesirable speckle which would mask the desired signal. In addition, SLAM required a fairly highly reflective surface to generate a measurable signal at the detector. These difficulties were overcome by placing a mirrored coverslip on top of the specimen being studied. This method was previously proven successful for testing unpolished silicon carbides and silicon nitrides [55,56]. However, one aim of nondestructive testing is to perform the testing or measurement without measurement-instrument induced damage to the specimen. Intimate contact of the coverslip with the specimen could theoretically produce surface damage to some materials. Therefore, the coverslip was placed slightly above the surface of the specimen at all times. It should also be noted that the presence of the coverslip added an element for acoustic attenuation to the system and complicated the analysis of the final data.

There were primarily three phases to the experimental research. In Phase I, the existing SLAM system was evaluated as a function of operating conditions in terms of its resolution and attenuation characteristics. This provided a characterization of the baseline system performance. The optical response of the

system as a function of spatial frequency yielded a measure of the system modulation transfer function (MTF) and indicated system operation in service [57].

In Phase II of the research, a model for the measurement of strain was proposed and experimentally verified. This in situ strain measurement capability required system modifications to the existing SLAM design. The modified SLAM was used to measure the in situ tensile strain of small diameter ceramic fibers. The fiber test specimens studied were primarily Nicalon β-silicon carbide (SiC). (However, due to current interest in Carborundum α-SiC and Saphikon single crystal α-alumina (Al_2O_3) fibers for elevated temperature applications, these fibers were also analyzed. The results of the studies on these fibers are presented independently of this work [58,59]).

Phase III of the research entailed the measurement of the local strain induced in glass ceramics and glass ceramic matrix composites under four-point flexural loading. The ceramic test specimens used were glass ceramic lithium alumino-silicate (LAS) monolithics, LAS/Nicalon SiC monofilament composites, and calcium alumino-silicate (CAS)/Nicalon SiC fully-reinforced unidirectional composites provided by Corning Glass Works.

Phase I: SLAM System Evaluation

The SLAM[1] was evaluated in terms of resolution and attenuation response as a function of the operating frequency. For the resolution studies, an Air Force Resolution test target was used as the object in the SLAM acoustic operating mode. The test chart is a chrome on glass target having line sets of varying periodicity (see Figure 3). The SLAM piezo-electric transducer operating at the desired frequency was covered with deionized water and the test target was placed in intimate contact with it. The scanning HeNe laser beam was raster scanned over the region of interest on the target. The resolution was measured at the selected frequency. The resolvable separation of the chrome lines on the target, using the Rayleigh criteria [60], defined the measured system resolution. This procedure was performed at nominal frequencies of 10, 24, 30, and 100 MHz. The measured and theoretical resolution based on diffraction theory were plotted as a function of frequency.

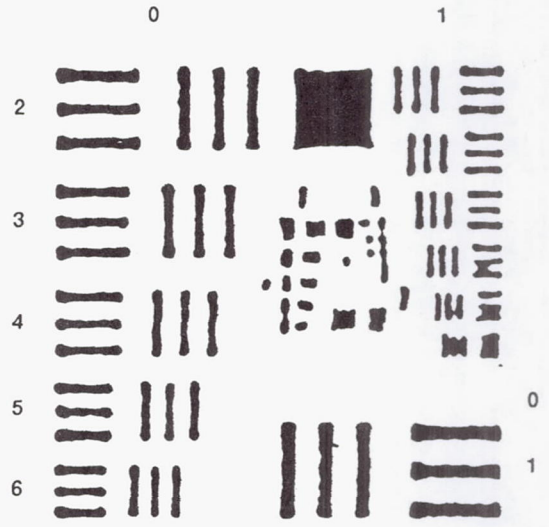

Figure 3.—Air Force test chart.

[1] Sonoscan, Inc. Model 2140

Each material has a characteristic acoustic response dependent on its scattering and resonant properties. The acoustic response is frequency dependent and a study of the acoustic response of the material was necessary to determine the optimal frequency regime with which to study each specimen class. The LAS and CAS/SiC specimens were tested for their attenuation characteristics as a function of frequency. The specimen of interest was placed in intimate contact with the water covering the transducer operating at the desired frequency. The SLAM "sonometer" registered the acoustic intensity level transmitted through the specimen. This level was noted with respect to a predetermined reference level. The specimen was removed from the transducer assembly and the new intensity level was noted. Known values of electrical attenuation were placed in the signal path to reduce the intensity level to the previous value. The total electrical attenuation was equivalent to the acoustic attenuation of the sample. This procedure was repeated at nominal frequencies of 10, 24, 30, and 100 MHz for each specimen. The measured data were plotted as a function of frequency. A determination of the optimal frequency regime at which to perform the experimental studies for each material system was based on the relative attenuation data and the corresponding acousto-optical signal response received at the detector.

Phase II: Strain Measurements of Ceramic Fibers

The Nicalon β-SiC fibers used for this study were provided by DOW-Corning. The fiber characteristics and properties are described in detail in references 61 and 62. The published procedures for processing Nicalon fiber [63,64] and results of pertinent fiber characterization studies are summarized in Chapter IV.

Fifteen individual as-received Nicalon fibers were evaluated for their tensile strain with the SLAM measurement system. The individual fibers were mounted with epoxy on 0.0254 mm (0.001") thick stainless steel shim stock tabs as shown schematically in Figure 4. The tabs were machined to yield a one-inch gauge length specimen configuration. One end of the tab was secured to the SLAM stage with a screw mechanism. A calibrated static load was applied to the other end of the tab via a frictionless air bearing pulley assembly designed to minimize the losses due to frictional effects between the SLAM stage and the shim tab. The tab was cut, as indicated in Figure 4, to ensure load transfer to the fiber test specimen. The experimental configuration is shown in Figure 5. A small drop of deionized water was placed between the piezo-electric transducer and the specimen. The water was an acoustic couplant which promoted more effective acoustic transfer from the piezo-electric crystal to the specimen. A mirrored coverslip was placed 0.0254 mm (0.001") above the specimen to increase the reflectivity of the optical signal response. The acoustic couplant was used as an interface between the specimen and the coverslip.

The spot size of the laser beam at the specimen surface was set to 22 μm at the specimen surface. The SLAM system raster scanned the laser over a 2.5 x 3.0 mm area located at the center of the specimen gauge length. This denoted the fiber region of interest (ROI) for measurement.

The optical signal from the SLAM interference fringes of the ROI received at the detector plane was directed to a 100 MHz oscilloscope. The raster line at the location of the fiber test specimen was selected and the normalized fringe shift was measured directly from the analog signal on the scope. Fringe shift tracking was performed by aligning the peak of the fringe of interest with the time base reference cursor on the oscilloscope; the phase shift cursor was aligned with the peak of the fringe after the fiber was stressed to the appropriate level. The delta between the two cursors in the time domain gave a measure of the fringe shift. The normalized fringe shift was calculated by dividing the measured time base fringe shift by the peak-to-peak separation of the fringes in the time domain. Using the measured normalized fringe shift in the strain measurement model (Appendix C), the tensile strain on the fiber was calculated.

In this study, only subcritical stress levels were applied to the fibers during strain testing. A random sample of the as-received fiber specimens having one-inch gauge lengths were tested for their tensile strength in a Universal Tester[2] operating

[2] Instron Corp. Model 4502

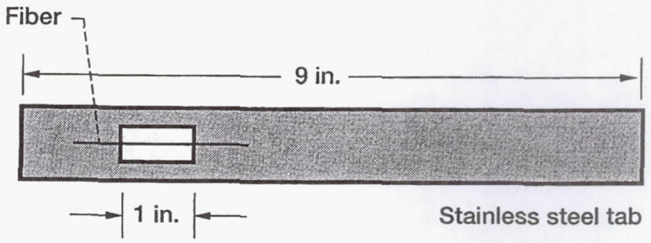

Figure 4.—Fiber test specimen configuration.

at a crosshead rate of 0.0085 mm/sec (0.02"/minute). The applied stresses used during the strain measurement procedure were less than one-half of the measured mean tensile strength of the Nicalon fibers.

The angle of insonification in the SLAM configuration was set at 10 degrees. The piezo-electric crystal operated at 100±4 MHz. The parameters and the velocity of sound through the material were used to calculate the effective wavelength within the material structure. The velocity of sound through the Nicalon fiber was assumed to be approximately equal to the velocity reported in previous literature through fully dense bulk silicon carbide [65]. An estimate of the strain-optic coefficients for β-SiC was selected from tabulations found in the literature [66,67].

The strains for fifteen individual Nicalon fibers were measured at three arbitrarily selected load levels (10, 15, and 20 grams). The maximum load level was chosen to ensure subcritical specimen loading, i.e. the maximum applied stress during strain measurement was less than one-half of the mean tensile strength of the Nicalon

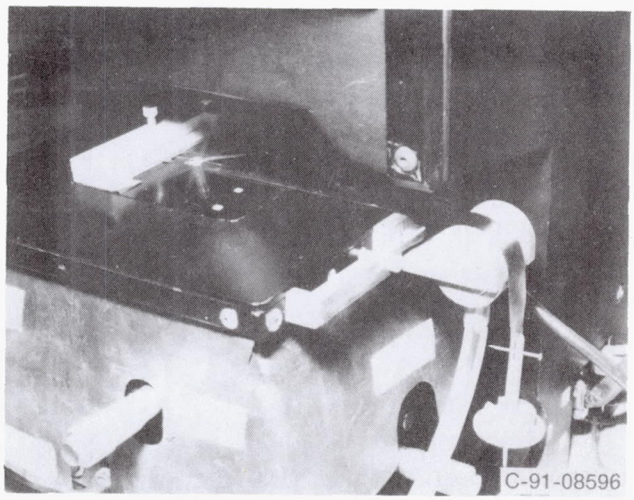

Figure 5.—Configuration for fiber strain measurement.

fibers. Following the strain measurement procedure, the fibers were removed from the SLAM system and the diameter of each was optically measured by a laser diffraction measuring system[3]. Measurements were made at twenty equispaced locations along the fiber length. The resultant mean diameter was used to compute the applied stress on the fiber at a specified load level such that, in MKS units,

$$\sigma_a = \frac{9.8\,P}{\pi\left(\frac{\phi}{2}\right)^2} \qquad (6)$$

where σ_a represents the applied stress (in Pascals), P is the measured applied load (in kilograms), and ϕ is the mean fiber diameter (in meters).

[3] United Calibration Corp.

The data were analyzed using a complete randomized block experimental design. The elastic modulus calculated at each measurement point formed a three by fifteen experimental matrix. In this design, the fiber to fiber variation was normalized and the residual variance was used to estimate the measurement uncertainty. This uncertainty yielded a measure of the reliability of the individual measurement. For each fiber, the strain data were plotted on stress-strain curves and the elastic modulus of the individual fibers was calculated by the method of linear regression. The elastic modulus measurements reported in the literature [63] were used as a basis for comparison.

The fracture surfaces of a representative sample of the Nicalon fibers were analyzed in the scanning electron microscope[4] (SEM). The resulting micrographs were compared with the nondestructive strain analysis results for interpretation of the data.

Phase III: Strain Measurements of Ceramic Composites

Lithium alumino-silicate (LAS) monolithic and monofilament fiber reinforced glass ceramic, and calcium alumino-silicate (CAS) glass ceramic matrix composite specimens reinforced with Nicalon SiC fibers were investigated in this study. Twenty specimens of each system described in Chapter IV were evaluated. For each system,

[4] Jeol Model JSM-840A

ten specimens were used for initial as-received characterization studies. The flexural strength of the specimens was measured with a Universal Tester[5]. The flexure bars were tested in the four-point flexure configuration shown in Figure 6 at a crosshead rate of 0.0085 mm/second (0.02 inches per minute).

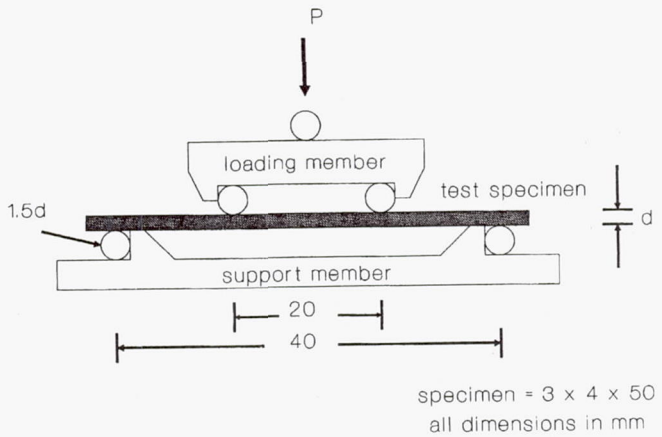

Figure 6.—Four-point flexural test configuration.

The remaining unfractured specimens were nonintrusively tested. The specimens were placed in the SLAM as shown schematically in Figure 7. The specimen was placed in a four-point flexure fixture using a modified design to that previously described for the initial strength testing. The modified fixture designs are shown in Appendix D. The fixture was designed to be placed in the SLAM to allow in situ stressing of the specimen. The base of the specimen was in intimate contact with the reservoir of deionized water required in the SLAM for effective acoustic

[5] Instron Corp. Model TTC-LM1

wave transfer from the transducer to the specimen. The load was applied parallel to the table surface such that the entire flexure assembly was rotated ninety degrees from its standard configuration (Figure 6). Single point loading was applied to the specimen via a screw mechanism through the upper arm of the future-bracket.

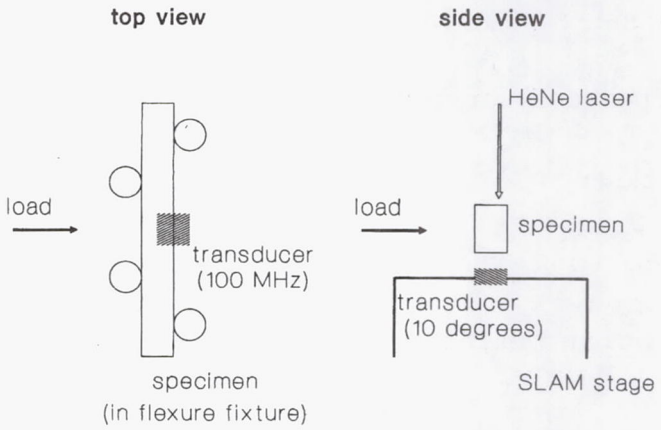

Figure 7.—Four-point flexure configuration in SLAM.

The fixture was made from 17-4 precipitation hardened stainless steel (hardness RC-50) to prevent corrosion due to contact with the water. The assembly was aligned and held in place on the SLAM stage by mechanical attachment.

The applied load was measured with a quarter-inch diameter compression load cell. A resistance strain gauge was attached to the load cell. The strain of the load cell was registered using a strain indicator[6]. The load cell was calibrated in the Instron universal tester prior to use. The registered strain on the gauge was recorded

[6] Measurements Group Model 3500A

at known load levels applied to the load cell. A calibration curve relating registered strain to applied load was constructed. Measurement of the load applied to the test specimen was then performed by placing the calibrated load cell in the fixture and directly measuring the registered strain on the load cell. The calibration curve was used to convert the measured strain to load.

Assessment of the strain from the SLAM fringe shift data required a measure of the velocity of sound propagation through the test specimen. The acoustic velocity was measured independently for each material, prior to strain testing, using the pulse echo contact technique to obtain ultrasonic data [68,69,70]. A schematic of this technique is shown in Figure 8. An ultrasonic pulse was sent through the test specimen. As the wave travelled through the test specimen, it was partially reflected

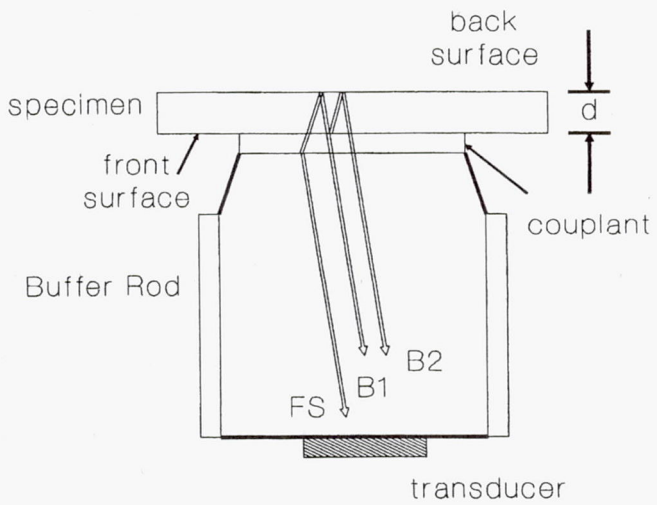

Figure 8.—Pulse echo setup for ultrasonic velocity measurement.

at the buffer rod-couplant-specimen interface (FS) and partially reflected off the back surface (B_1). Similarly, echo B_2 represents the second back surface reflection of the ultrasonic wave. This ultrasonic pulse, travelling a distance twice the specimen thickness, integrates the microstructural information from the sample volume element. The size of the volume element was determined by the ultrasonic beam diameter [71,72]. The time shift, τ_0, between the two back surface reflection waveforms (B_1 and B_2) was determined by cross-correlation [69,73],

$$\tau_0 = \left| \lim_{T\to\infty} \int_{-T}^{T} B_1(t) * B_2(t+\tau)\, dt \right|_{-\infty\le\tau\le\infty} \qquad (7)$$

where t represents time and T is the time duration of the pulse. The cross correlation velocity was then determined as

$$v = \frac{2d}{\tau_0} \qquad (8)$$

where d is the thickness of the test specimen. For each material, the ultrasonic wave velocity was measured at three spatially separate locations along the specimen length to account for differences in the wave velocity due to variations in the microstructure.

The LAS monolithic strain measurements were made using a SLAM operating at a frequency of 100±4 MHz. The CAS/SiC composite strain measurements were made at an operating frequency of 30±2 MHz. (Due to limitations in the SLAM system used at the NASA Lewis Research Center, the lower frequency operation measurements were performed by Sonoscan, Inc.) The angle of insonification was

set at 10 degrees. The specimen assembly was positioned such that the test region of the specimen was the maximum tensile zone as shown in Figure 9. As the specimen was stressed, the accumulation of damage within the ceramic strained the matrix. The alteration of the strain profile at the maximum tensile zone was measured. Photographs of the images of select SLAM interferograms were taken to demonstrate the altered mode as damage accumulated in the specimen.

At each region of interest (ROI), an initial interferogram was taken from the SLAM prior to loading of the specimen. This interferogram served as the reference with respect to which the measurements were made. The specimen was loaded to a series of predetermined, arbitarily selected load levels (6.0, 8.5, 11.0, 15.0, 16.5, 18.0, and 20.0 lbs). This selection of loads ensured that the maximum applied stress was subcritical in relation to the experimentally determined flexural strength. An additional experiment was conducted to ensure the independence of the measured data on the maximum applied stress. In this experiment, three LAS MOR specimens were loaded, as described above, to maximum applied loads of 16.5, 18.0, and 25.0 lbs. Strain measurement and analysis was performed by similar procedures for all loading levels.

Subsequent SLAM interferograms were taken with the load applied. After the specimen was loaded to its maximum state of stress for measurement, the load on the specimen was released to its initial stress state. A final interferogram was taken.

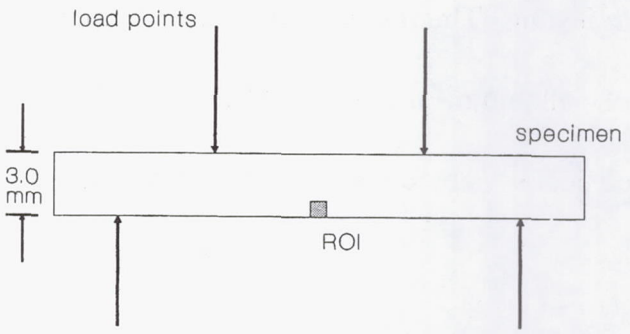

Figure 9.—Region of interest for flexural test specimens.

The strain measurement was made by measuring the normalized fringe shift of the analog signal of the interferograms displayed on the 100 MHz oscilloscope between the stress states of interest. The fringe shift was measured directly from the analog signal in the time domain by placing the time base reference cursor from the oscilloscope on the peak of the fringe of interest at the initial stress state; the phase delay cursor was placed on the peak of the shifted fringe after the test specimen was stressed to the specified level. The time delay between the cursor positions yielded the fringe shift measurement in the time domain. The normalized fringe shift was calculated by dividing the time based fringe shift by the peak-to-peak separation of the fringes. This normalized fringe shift was used to determine the strain within the ROI, as described in Appendix C. This process was repeated for each specimen.

Each specimen was individually marked for identification prior to testing. After nondestructive strain testing was completed, the strength under four-point

flexural loading of the remaining specimens was measured on the TTC universal tester. A representative sample of each group of specimens were identified for SEM analysis after strength testing. The fracture surfaces of each of these specimens were coated with 10 nm of palladium for enhanced SEM imaging.

The measured loads were used to calculate the applied stress on the test specimen as,

$$\sigma_a = \frac{3\,P\,a}{b\,d^2} \qquad (9)$$

where σ_a is the applied stress, P is the applied load, a is the inner-to-outer span dimension on the fixture (10 mm, in this case), b is the width of the test specimen (4 mm), and d is the height of the test specimen (3 mm, unless otherwise noted as described in Chapter IV). These stress values and the SLAM strain measurements were used to generate stress-strain curves for each specimen studied. The measured local strain values were compared with the destructive strength testing results on a specimen to specimen basis. This comparison allowed a quantitative relationship to be drawn between the nondestructive and destructive analyses which could be explained in terms of microstructural parameters and fracture behavior.

CHAPTER IV

SPECIMENS AND SPECIMEN PREPARATION

The specimens used for this research program were fiber-reinforced glass ceramic matrix composites of varying degrees of complexity. The constituents of the composites were also analyzed to provide a quantitative foundation for the analysis of the composite system. The specimens studied include:

1. Nicalon SiC fiber
2. lithium aluminosilicate (LAS) glass ceramic
3. LAS matrix with a Nicalon SiC monofilament
4. calcium aluminosilicate (CAS) matrix / Nicalon SiC FRC

The LAS and CAS specimens were provided pre-fabricated by Corning Glass Works. The LAS/SiC monofilament composites were prepared by the University of Dayton Research Institute using the as-received LAS bars and Nicalon fibers.

The Nicalon fiber used in this study was provided by Dow-Corning. The fiber characteristics and properties have been extensively studied and reported in previous work [61,74]. In the fiber preparation process, dimethyldi-chlorosilane is dechlorinated and polymerized to a polycarbosilane. The polycarbosilane is spun into fibers and

pyrolized to β-SiC. The spun fibers are coated with a vinyl acetate sizing resin. The final fiber is nonstoichiometric, composed of β-SiC crystallites with excess carbon and approximately 10 percent oxygen, present as SiO_2. The fibers supplied by Dow were in a 500 meter spool of tow bundles consisting of ~ 500 fibers per tow. The nominal diameter of the individual fibers was specified at 15 μm. Pertinent mechanical properties of the Nicalon fiber (reported by the manufacturer) are listed in Table 1 [63].

The fiber is also oxidation and corrosion resistant and has been investigated for elevated temperature applications [75]. However, the lack of stoichiometry of the Nicalon fibers leads to variations in the microstructure along the fiber length and among different fibers [76]. In addition, large variations in the fiber diameter are often observed [77].

Table 1: Typical Properties for 15 μm Nicalon β-SiC Fiber

Property	Average Value
Density, g/cc	2.55
Tensile Strength, GPa	2.96
Elastic Modulus (E), GPa	190
Strain to Failure (ϵ), %	1.5
Poisson's Ratio (ν_{12})	0.3
Thermal Conductivity,	10
Coeff. of Therm Exp. (α), C^{-1}	4.0×10^{-6}

Studies performed at the University of Dayton Research Institute indicate that the strength of the Nicalon fibers drops precipitously at elevated temperatures in vacuum. Their findings show that this was due to significant outgassing of carbon monoxide from the fiber at temperatures above 1200°C in vacuum [61]. This behavior is critical in determining the appropriate processing conditions for the manufacture of the ceramic composites.

Categorically, glass-ceramics are produced by the controlled crystallization of the appropriate glass composition. In order to form the small grain size desirable for glass-ceramics, a high density of nuclei is required; nucleating agents are added to the glass and appropriate heat treatment effects the nucleation and growth to form the glass ceramic [11]. The Corning Glass Works' LAS frit is typically manufactured by combining Li_2O_3, SiO_2, Al_2O_3, and approximately 2% nucleating agent. The nucleating agent used in the manufacturing process of the LAS supplied by Corning is TiO_2. The constituents are melted and quenched with water to form the frit. The mixture is then ball-milled to form a glassy powder of approximately 12 μm particle size. The LAS powder, in this form, is commercially described as Corning Glass Works' 9608.

The LAS frit was used to prepare glass ceramic compacts at Corning Glass Works [11] which were purchased from a commercial distributor for this project. These as-received LAS compacts were cut and ground to the appropriate size for

modulus of rupture (MOR) specimens (according to Military Standard 1942A for flexure testing [78]) at the University of Dayton Research Institute. These LAS bars contain inherent internal stresses due to processing as described in Chapter II.

The single fiber composite specimens were hot pressed directly from the LAS bars and as-received Nicalon fibers. The hot-pressing atmospheric processing conditions used were refined from recommendations by United Technologies Research Corporation (UTRC) based upon their earlier work [79]. MOR bars of 3mm x 4mm x 50mm dimension (Mil-Std 1942A) were prepared from the hot-pressed billets. The reinforcing fiber was aligned with the long axis of the bar and was located at the midline of the tensile region of the specimen as shown in Figure 10. In this configuration, when the composite specimens were stressed in four-point flexure, the reinforcing fiber was in tension. This tensile region of the matrix surrounding the fiber was the region of interest for measurement.

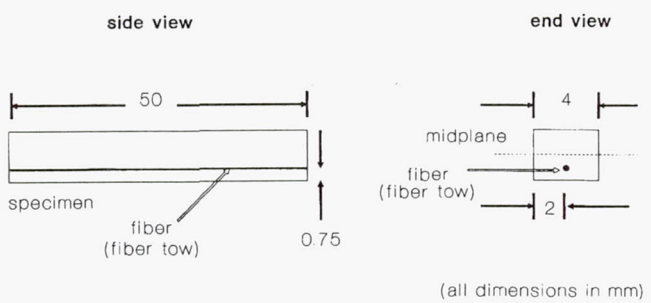

Figure 10.—Monofilament ceramic composite.

Specimen preparation required that the glass ceramic compact and fiber be arranged in their final positions prior to hot pressing. An array of three equispaced 0.102 mm (0.004") grooves were scribed in a 0.75 mm (0.029") thick by 50.8 mm (2.0") square glass ceramic plate as shown in Figure 11. A single Nicalon fiber was lain in each groove and held in place with wax adhesive. A 2.25 mm (.088") thick by 50.8 mm (2.0") square glass ceramic plate was placed over the bottom plate. The notches in the plate provided supports for the Nicalon fiber to prevent kinking and misalignment during hot pressing.

The Nicalon fiber and specimen material were heated in a nitrogen atmosphere to 1280°C. (The tendency of the Nicalon fiber to outgas at high temperature in vacuum may cause undesirable bubbles to form in the composite matrix during densification. This problem was minimized by preheating the Nicalon fiber material to release any gases prior to the densification process and by performing the densification in an inert atmosphere.) The disks were hot-pressed at 200 psi for 10 minutes at the 1280°C temperature. These conditions allowed the glass ceramic near the fiber to flow and form an effective composite interface around the fiber as the material devitrified during cool down. These billets were cut and ground to 3mm x 4mm x 50mm test bars such that each specimen contained a single fiber. The final location and orientation of the fiber in the matrix was shown in Figure 10.

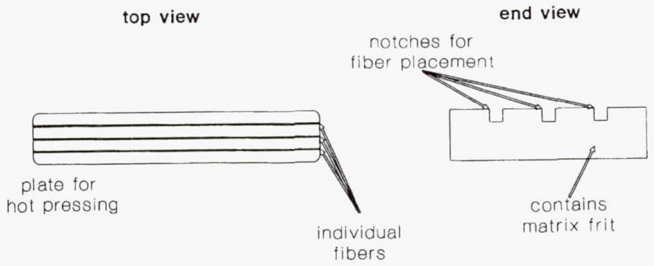

Figure 11.—Schematic describing preparation of monofilament composite.

The CAS/SiC specimens were cut and ground to the desired MOR specifications (2mm x 4mm x 50mm) from the billets of CAS with unidirectional Nicalon reinforcing fibers. The exact composition and processing procedures of the CAS specimens are proprietary to Corning and have not been disclosed. We also agreed not to analyze the material for its composition or properties other than for the express purpose of this research.

However, unidirectional fiber reinforced glass ceramic composites are typically processed by similar procedures. The sizing coating on the Nicalon fibers is removed by passing the tow of fibers used for reinforcement under a flame. The tow is separated into its individual fibers which are dipped in a slurry of the glass composition (CAS) and then wrapped on a drum to dry. A single sheet of the glass reinforced with fibers is formed and cut to the size appropriate for hot pressing. Alternating layers of these fiber reinforced sheets and CAS glass frit are stacked to

establish the desired volume fraction of fibers in the glass ceramic matrix. Typically, the fiber volume fraction for unidirectional fiber reinforced glass ceramic composites is approximately 35 percent. The layered section is hot pressed to densify the composite structure.

This processing procedure for the composite structure leads to the generation of internal residual stresses as described in Chapter II. Typical properties found in the literature for LAS and CAS glass ceramics are given in Table 2 [11,47,80]. MCS is the matrix cracking stress, i.e., the stress at which the first matrix cracking occurs, as predicted by the Aveston et al. (ACK) model and Marshall et al. (MCE) model (Appendix A). The MCS reported refers to a unidirectional composite of the matrix indicated reinforced with Nicalon SiC fibers. The fiber volume ratio (V_f) is assumed to be 50 percent for LAS/SiC and 35 percent for CAS/SiC.

Table 2: Typical Properties for LAS and CAS Glass Ceramics

Property	LAS	CAS
Elastic Modulus (GPa)	88	88
Fract. Toughness (MPa $m^{½}$)	2	N/A
Density (g/cm^3)	3.20	2.60
Coeff Therm Exp. ($x10^{-6}$ C^{-1})	par. c-axis -2.0 perp. c-axis 6.5	5.0
τ (MPa)	3	7
γ (J m^{-2})	40	40
Composite MCS (MPa)	265	376

CHAPTER V

RESULTS AND DISCUSSION

Analysis of the acousto-optical response from the scanning laser acoustic microscope signal allowed in situ quantitative mechanical behavior characterizations of small diameter ceramic fibers under tensile loading. It also provided a methodology for the local analysis of ceramics and ceramic composites under flexural loading. Such analysis provided concurrent quantitative and qualitative interpretations of the material structure and substructure. The high diffraction-limited resolution capability of the SLAM system allowed localized analyses of the materials. This permitted an effective assessment of the correlation between mechanical behavior and microstructural features.

Due to the extensive nature of the unprocessed SLAM measurement data, the strain measurements for each material system are included as appendices to the main text. Each relevant appendix will be called out in the corresponding sections of this chapter.

Resolution and Attenuation of SLAM

The measured resolution of the scanning laser acoustic microscope (System 2140) is shown as a function of the operating frequency in Figure 12. The resolution of the SLAM system was diffraction limited. As described in Chapter II, the frequency dependence of resolution for a diffraction limited system is described by equation (5). This dependence (calculated using tabulated values for the velocity of sound propagation) is shown as the theoretical curve in Figure 12. The resolving capability of the system increased with increasing frequency; at higher frequencies, it was possible to resolve smaller structures. Therefore, for very high resolution work, the highest operating frequencies are desirable.

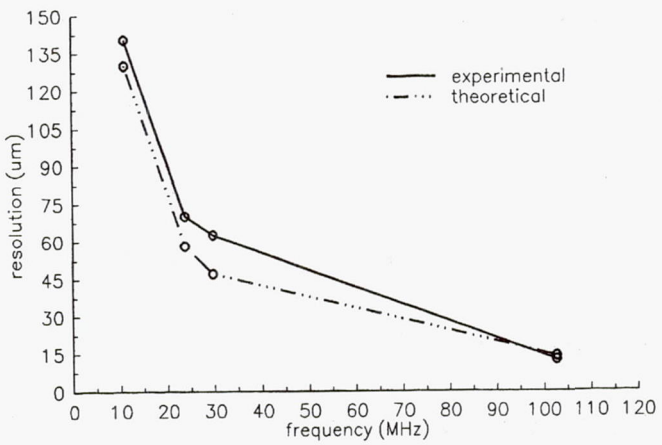

Figure 12.—System resolution of SLAM.

In the frequency regime of most of the experimental studies presented in this work (100±4 MHz), the measured resolution for the chrome on glass Air Force resolution test chart (Figure 3) was 11 μm. At this resolution, the analysis of materials having dimensions to 11 μm is allowed. This is particularly germane to this dissertation since it implies that the 15 μm diameter Nicalon fibers can be tested.

The measured attenuation characteristics for LAS monolithics and CAS/SiC composites are shown in Figures 13 and 14, respectively. The attenuation of each specimen increased with increasing frequency, as is characteristic of attenuation due to scattering [81]. This implies that an operating frequency for specimen testing must be chosen such that a tradeoff is made between resolution and attenuation. If the specimens being studied are highly attenuating, a lower operating frequency must often be selected for analysis. This yields poorer attainable resolutions. Operating frequency selection is typically based on the sample set being studied and its characteristic attenuation, and the required specifications of the measurements.

For the purposes of this study, resolution was the critical parameter for the fiber specimens. The fiber test specimens did not develop significant attenuation of the acoustical wave through the specimens due to their small transverse dimensions (15 μm). However, a resolving capability of at least 15 μm was required to analyze the strain distribution of the Nicalon fibers. Therefore, an operating frequency of 100 MHz was selected for the Nicalon fiber test specimens.

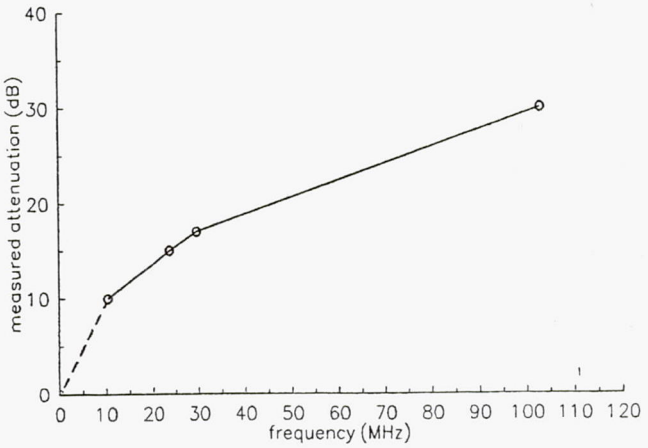

Figure 13.—Measured attenuation characteristic of LAS.

The limiting parameter for the strain analysis of the LAS monolithics and the CAS/SiC composites was the attenuation of the ultrasonic wave through the test specimen. Test specimens having small grain sizes such as LAS (on the order of 10 μm) are prone to extensive scattering of ultrasonic waves. Further, highly porous materials are subject to a high degree of absorption of the ultrasonic wave. The LAS used for this study was, however, fully dense and the attenuation curve shows that operating frequencies of 100 MHz can be used to achieve higher resolutions.

The CAS/SiC specimens were subject to greater attenuation of the acoustic wave due to phonon scattering at the fiber-matrix interfaces. The internal acoustic scattering in the FRCs was sufficient to extensively attenuate the intensity of the signal received at the detector and significantly degrade the signal-to-noise ratio

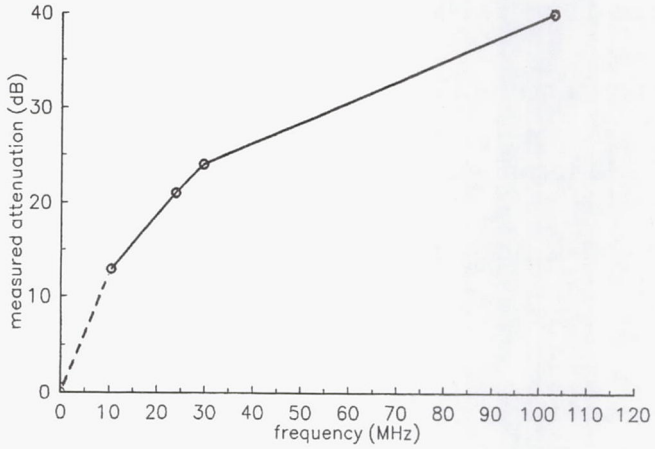

Figure 14.—Measured attenuation characteristic of CAS/SiC.

(SNR). In terms of the observed acoustic image, this scattering gave rise to acoustic speckle. When there was too much scattering in the specimen, the acoustic speckle masked the desired signal.

The measurement capability of the highly attenuating CAS/SiC specimens could be provided by employing a lower operating frequency. The CAS/SiC composite strain analysis was performed at 30±2 MHz, thereby degrading the optimal system resolution. This indicated that while strain measurements of FRCs using SLAM were viable, practical application for high resolution work was limited to simple systems such as fibers and monolithics.

Strain Analysis of Ceramic Fibers

The SLAM measurement technique provided quantitative in situ tensile strain analyses of the 15 μm diameter Nicalon fibers. This characterization was critical to determining the performance of the Nicalon fiber but it was also testimony to the reliability of the SLAM technique for high resolution strain measurement. The 15 μm nominal dimension is near the optimum system resolution at the operating frequency of 100 MHz (11 μm). Measurement and characterization of the Nicalon fiber represented an analysis near the system's limit of resolution.

An optical micrograph showing the typical interference fringes resulting from the acousto-optical response of a Nicalon fiber is shown in Figure 15. The fiber is indicated by the arrows in the figure. The medium surrounding the fiber is the water couplant. As the fiber was stressed to the predetermined subcritical load levels, the interference fringes shifted, producing a measure of the strain on the fiber. The unprocessed strain data obtained for each fiber are tabulated in Appendix E.

Figure 16 shows a plot of the typically observed stress-strain behavior obtained for an individual fiber. The error bars shown were propagated from the measurement uncertainties and the errors due to assumptions about the available constants. The propagated measurement error was less than five percent of the absolute strain measurement. The elastic modulus values obtained from the linear regression analysis of the stress-strain data for the fifteen Nicalon SiC fibers are

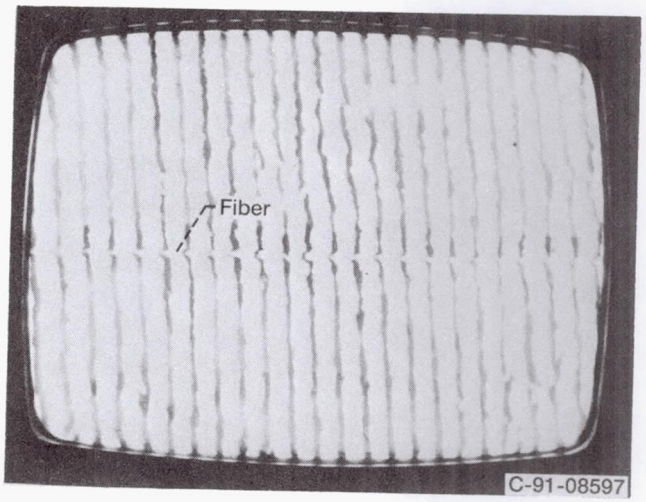

Figure 15.—Interference fringes from Nicalon SiC fiber.

tabulated in Table 3. For the fifteen fibers studied, the mean elastic modulus, calculated from a linear regression of the measured stress and strain, was 185.3±2.6 GPa (26.9±0.4 Msi). This compared favorably with the elastic modulus value of 193.0 GPa (28.0 Msi) reported in the literature (within 2.8 percent). The reported uncertainty represents the propagated measurement uncertainty from the experimental data.

The standard deviation of the elastic modulus measurements was 22 GPa (3.2 Msi), approximately 12 percent about the mean. However, this standard deviation included effects of the fiber to fiber variations and random variations in the measurements. The complete randomized block analysis of the raw data was used to assess the statistical significance of any real differences between the fibers. Using

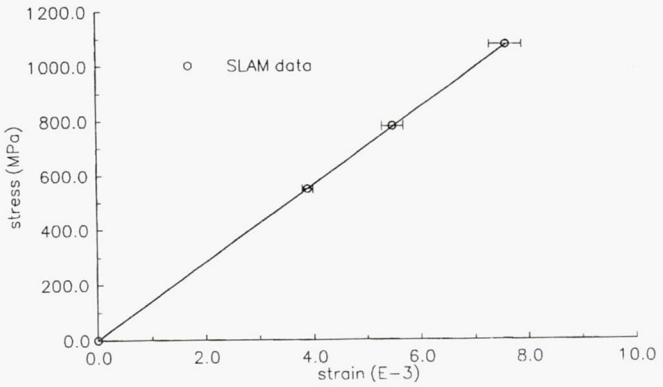

Figure 16.—Stress-strain behavior for 15 μm Nicalon β-SiC fiber.

the elastic modulus calculated at each measurement point as the experimental matrix, this analysis indicated that there was a statistically significant variation in the measured elastic modulus from fiber to fiber. This variance was primarily attributed to subtle differences in the microstructure from fiber to fiber. As was discussed in Chapter IV, the Nicalon fiber is a nonstoichiometric compound consisting of β-SiC crystallites suspended in an amorphous matrix. This leads to microstructural variations between fibers, even within the same tow [76,77].

There are also indications of variations in the fracture surface topology of various Nicalon fibers as is shown in the SEM micrographs in Figure 17. The fracture surface of one Nicalon fiber (Figure 17a) has a flat texture while another Nicalon fiber from the same tow (Figure 17b) has a slightly more tortuous fracture

Table 3: Elastic Modulus Measurements for Nicalon β-SiC Fibers

Fiber	Measured modulus, GPa
1	185.3
2	189.2
3	187.9
4	172.1
5	153.4
6	210.3
7	145.5
8	210.4
9	199.6
10	193.8
11	214.6
12	151.6
13	187.9
14	183.3
15	194.0
Mean ± Sigma	185.3 ± 22.6

surface. The differences in the fracture surfaces may indicate small variations in the material substructure [82].

Variations in the measured modulus at the different load levels for a particular fiber was statistically insignificant and may be attributed to random measurement

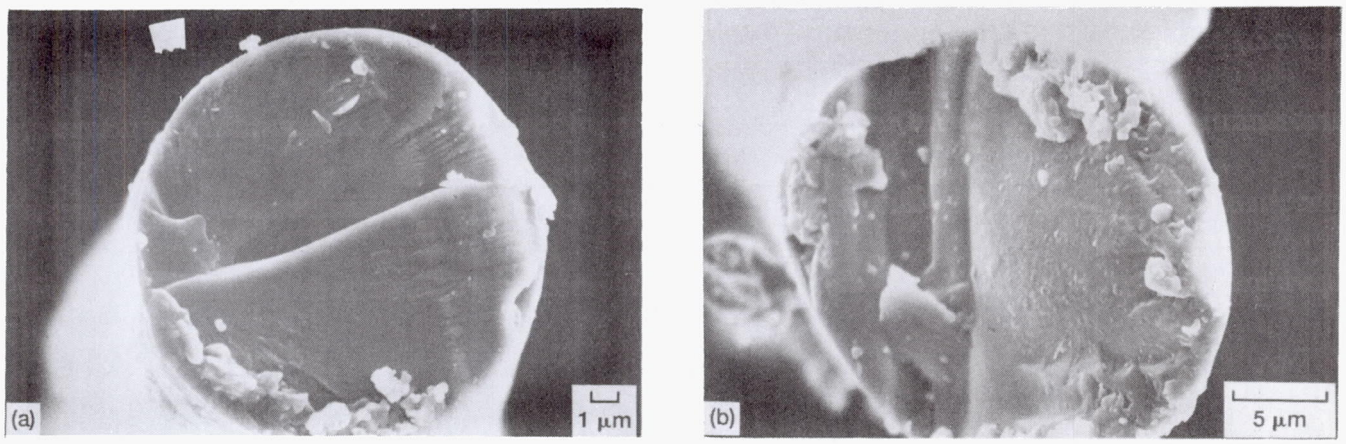

Figure 17.—SEM micrographs of fracture surfaces of Nicalon SiC.

deviations. Using a scaled t-distribution as a reference distribution, the analysis indicated that the estimated standard error of the mean due solely to random measurement variation was 2.6 GPa at a 95 percent confidence level. This indicated that the measurement technique was reliable across a statistical sample set, suggesting that the SLAM measurement technique was practical for use in on-line operation since it was not overly sensitive to subtle differences between specimens of a particular class.

The strain analysis of the Nicalon fibers indicated that the SLAM measurement technique was effective and accurate for measuring the in situ tensile strain of small diameter ceramic fibers. However, the velocity of sound through the

material and the strain-optic coefficients for the material were necessary parameters in the measurement model. These constants are measurable on bulk material but are difficult to assess directly for small diameter fibers [83]. In this work, it was assumed that the fiber constants could be determined by analyzing the bulk material. While this might introduce some inaccuracy to the final measurement, the processed data indicated that the error was not significant. In any case, the error introduced by employing these assumptions was systematic and could be easily removed by appropriate calibration to an accepted standard.

Strain Analysis of Ceramic Monolithics

The tabulated experimental measurements for flexural strength of the as-received Corning 9608 LAS bars are presented in Table 4. The measured mean flexural strength (MOR) of the as-received LAS bars was 113.0 ± 17.1 MPa (16.4 ± 2.5 ksi). The mean strength compared well (within 3.5 percent) with the median MOR value of 117.2 MPa reported in literature for LAS [11]. The reported uncertainty represents the standard deviation of the measured strength values across the sample set. This standard deviation is relatively large (approximately 15.1 percent about the mean flexural strength), as expected for ceramic monolithic materials whose strengths are dictated by the presence of inherent flaw populations [84].

Table 4: Measured Strengths of LAS in Four-Point Flexure

Specimen	Flexural Strength, MPa
1	119.0
2	111.2
3	98.3
4	104.8
5	116.8
6	99.0
7	89.0
8	141.6
9	111.2
10	139.4
Mean ± Sigma	113.0 ± 17.1

The unprocessed strain measurements from SLAM for the LAS specimens are given in Appendix F. These values represent the local strain measured within the ROI (Figure 9) as each specimen was stressed to a subcritical level. A measurable strain, denoted ϵ_r, was observed for each specimen upon release of the applied stress. A typical plot of the observed local stress-strain behavior is shown in Figure 18.

Classical elasticity theory predicts a linear stress-strain curve to failure for glass ceramic materials. The observed load-deflection curves recorded during flexural strength testing of the LAS test specimens were indeed linear to failure. These load-

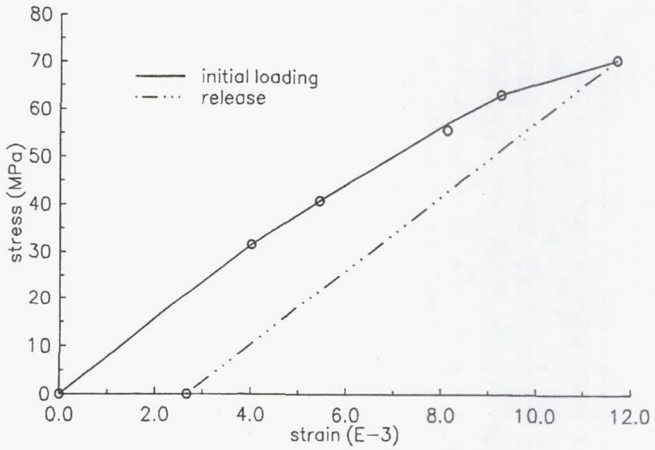

Figure 18.—Local stress-strain behavior of LAS in four-point flexure.

deflection curves represented the macroscopic mechanical behavior integrated over microstructural variations through the MOR bar. However, the typically observed SLAM stress-strain behavior within the ROI for the LAS was nonlinear, as shown in Figure 18. In contrast to the load-deflection curves, this stress-strain pattern is due to localized strain along the tensile zone. The local stress-strain behavior exhibited a notable nonlinear component, and apparent hysteresis upon unloading of the external mechanical stress. Releasing the specimen from a subcritical stress level induced a measurable strain, defined as "relaxation strain", greater than was present in the as-received specimen. The relaxation strain (ϵ_r) induced by external loading can be correlated to a relaxation stress (σ_r) level for each specimen, as shown schematically in Figure 19.

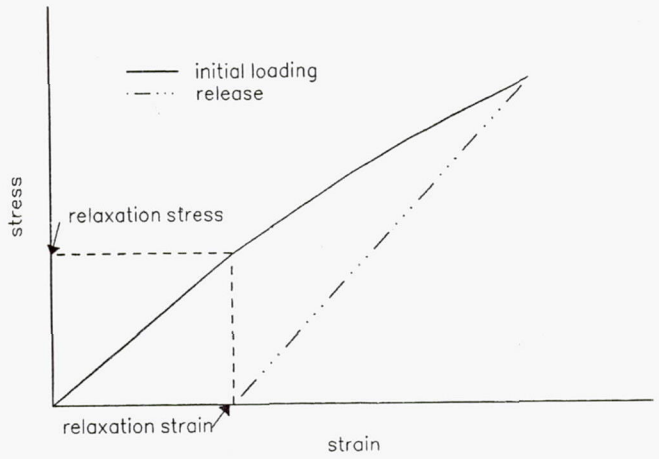

Figure 19.—Relaxation strain and stress.

The measured flexural strengths, relaxation stresses, and the local yield stresses (the stress at which departure from linearity occurs) for each LAS specimen tested in SLAM are tabulated in Table 5. This table also gives the ratio of the computed relaxation stress to the fracture stress for each specimen.

Table 6 presents the relaxation strain results for three LAS specimens unloaded at alternate applied stress levels. In each case, the measured relaxation strain was the same, within the uncertainty of the measurement. In addition, the ratio between the relaxation stresses and the fracture stresses for each specimen was 18.7 percent (statistically consistent with the results presented in Table 5). The relaxation strain and corresponding stress relaxation ratio are apparently independent of the subcritical stress levels applied to the specimens prior to unloading.

Table 5: Experimental Local Yield, Relaxation, and Fracture Stresses for LAS

Specimen	Yield Stress (σ_y), MPa	Rel. Stress (σ_r), MPa	Frac. Stress (σ_f), MPa	Ratio (σ_r/σ_f)
1	45	29.6	148.3	.200
2	55	20.0	115.0	.174
3	60	22.3	120.6	.185
4	61	23.6	139.8	.169
5	61	20.2	107.0	.189
6	61	14.8	92.7	.160
7	60	18.5	105.7	.175
8	55	22.5	106.4	.212
9	35	13.0	63.0	.206
Mean±Sigma	54.7±9.1	20.5±4.9	110.9± 25.4	.185± .018

The mean value of the flexural strength for the as-received (Table 4) and post-strain analyzed (Table 5) test specimens remained constant, within the measurement uncertainty, indicating that the nonintrusive SLAM measurement technique did not alter the ultimate fracture strength of the test specimens. The standard deviation of the flexural strength across the sample set was large in relationship to the mean (22.6 percent about the mean for the specimens tested in SLAM). As with the as-received specimens, the large variance was attributed to variations in the presence of inherent flaws, characteristic of ceramic test specimens.

Table 6: Relaxation Strain and Stress of LAS for Unloading from Selected Stress Values

Specimen	Stress at Unloading (MPa)	ϵ_r, (x 10^{-3})	Rel. Str. (σ_r), MPa	Frac. Str. (σ_f), MPa	Ratio (σ_r/σ_f)
1	55	3.53	28	152	.184
	67	3.42			
	83	3.53			
2	55	2.83	24	128	.188
	67	2.71			
	83	2.94			
3	55	2.85	24	118	.203
	67	2.85			
	83	2.96			

The mean local yield stress for LAS occurred at 55 MPa. In macroscopic behavior studies, many researchers regard the yield stress to indicate the onset of matrix cracking [39]. However, recent studies have shown that first matrix cracking actually occurs prior to yield [45,46,47] and the yield corresponds to steady state cracking [46]. In an analogous fashion, the local data indicate evidence of microcracking in LAS at 55 MPa but this stress level may not necessarily correspond to first matrix microcracking in the local domain.

The presence of the relaxation strain upon unloading indicated that, at the local level, the micromechanical behavior exhibited internal stress relaxation. In addition, the local stress-strain behavior suggests that energy was absorbed as damage accumulated. In this case, the damage did not lead to catastrophic failure but was sufficient to relieve the inherent internal stress in the material.

It is conjectured that due to the anisotropy of the coefficient of thermal expansion of LAS (6.5×10^{-6}/°C normal to the c-axis; -2.0×10^{-6}/°C parallel to the c-axis [38]), significant internal residual tensile stresses develop during the cool down stage of processing. The material seeks to reach its minimum energy stable configuration. However, the regions of high internal stress have large amounts of potential energy. This is a fundamentally energetically unstable condition. When small mechanical stresses are applied to the material, microcracks initiate in the high stress regions to relieve the system and achieve a more energetically favorable configuration. This results in multiple sites of fracture initiation and microcrack initiation. It is also reported in the literature that the occurrence of hackle on the fracture surface of glass ceramics can also be explained in terms of such microcrack propagation [85]. Appendix G outlines a mechanistic description of this phenomena.

The relaxation stress indicates an assessment of the local residual stress inherent to the material and accounts for the local nonlinear mechanical behavior. Independent researchers have reported analogous local mechanical behavior for other

ceramic systems; Lawn has observed local nonlinearities and toughening mechanisms in alumina [86] and Marshall has reported simliar localized effects in zirconia [87]. However, Marshall points out that the microcracks which form during local stress relaxation are not indicative of steady-state cracking behavior, i.e. the cracks are not independent of the stress intensity of the system. Therefore, once localized stress relaxation occurs, local interaction of the crack front with the microstructure is likely to dominate within the ROI and the local crack may be arrested. This suggests that the relaxation strain is not due to long-range deformation and therefore is not a function of the applied stress beyond that necessary to provide local stress relief [87].

For each individual specimen investigated, a definitive quantitative relationship between the measured relaxation stress and the fracture stress was found, as indicated by the ratios in Table 5. The mean ratio of the relaxation stress to the fracture stress was 18.5 ± 1.5 percent. The reported uncertainty represents the standard deviation of the processed data. Though the reported standard deviation of the fracture stresses for the specimens studied was large (22.6 percent), the standard deviation of the relative relaxation to fracture stress was much smaller (8.1 percent) across the sample set. This link between the two stresses implies that there was a definitive correlation between fracture stress and the relaxation stress, i.e. stress relief occurred at approximately 18.5 percent of the fracture stress of the LAS

material (20.5 MPa). Correlation of the relaxation and fracture stresses is consistent with the assertion that the relaxation effects coincide with non-steady state cracking.

This stress relaxation analysis indicated that there was a threshold for stress relief which occurred at 18.5 percent of the fracture stress for LAS. Similarly, a limited analysis of published LAS data indicated that the median threshold stress intensity occurred at approximately 20 percent of the mean fracture toughness value reported for LAS [88]. This similarity suggests that the mechanisms operating to produce the observed threshold effects may be analogous.

Figure 20 shows photographs of the images of the SLAM interferograms taken from the ROI (see Figure 9) with the specimen unloaded (Figure 20a), and loaded (Figure 20b) to the experimentally determined crack threshold stress. The arrows in the figures indicate the tensile surface of the MOR specimen. These photographs provide an example of the qualitative characterization capability of SLAM. A significant alteration of the interference mode and resulting signal response occurred once this threshold stress level was attained. The as-received specimen showed interference fringes which were straight and parallel, indicative of a homogeneous structure (Figure 20a). When cracks began to propagate, inhomogeneities were introduced to the specimen structure and the interference fringes exhibited an alteration of their relative orientation in the LAS specimens, as shown in Figure 20b. In addition, the relative spacing of the fringes was altered, indicating the occurrence

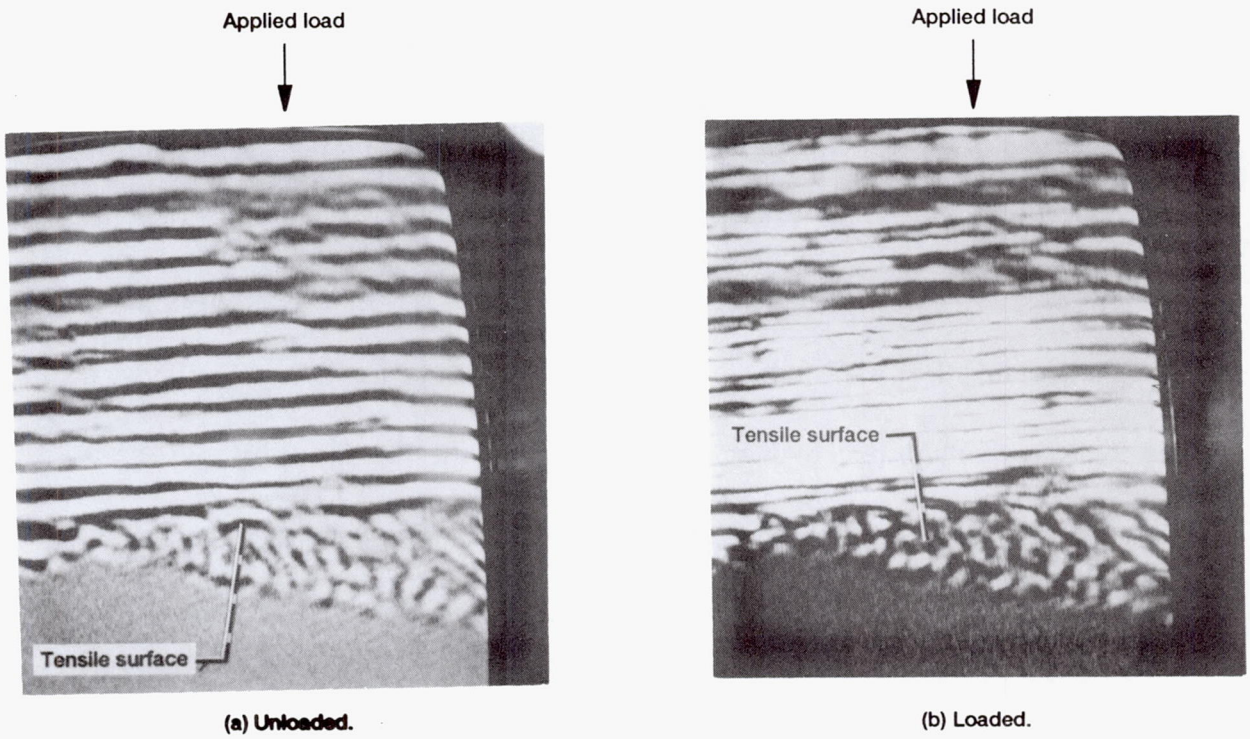

Figure 20.—SLAM interferograms of LAS.

of a fundamental change in the material's microstructure. This corroborated, on a qualitative basis, the occurrence of local stress relief.

Figure 21 shows the SEM micrographs for the tensile region of the fracture surfaces of two LAS bars. Figure 21a shows the fracture surface near the tensile side of one fractured specimens. The occurrence of multiple initiation sites along the tensile side of the bar is observed. The fracture surface of the specimen in Figure 21b shows a significant amount of microcracking and secondary cracking off the primary crack path. A large number of local initiation sites also occurred along the tensile zone of the fracture surface. It should be noted that each LAS specimen exhibited rather atypical fracture surface morphology. Clearly distinctive mirror zones surrounding fracture initiation sites were not evident.

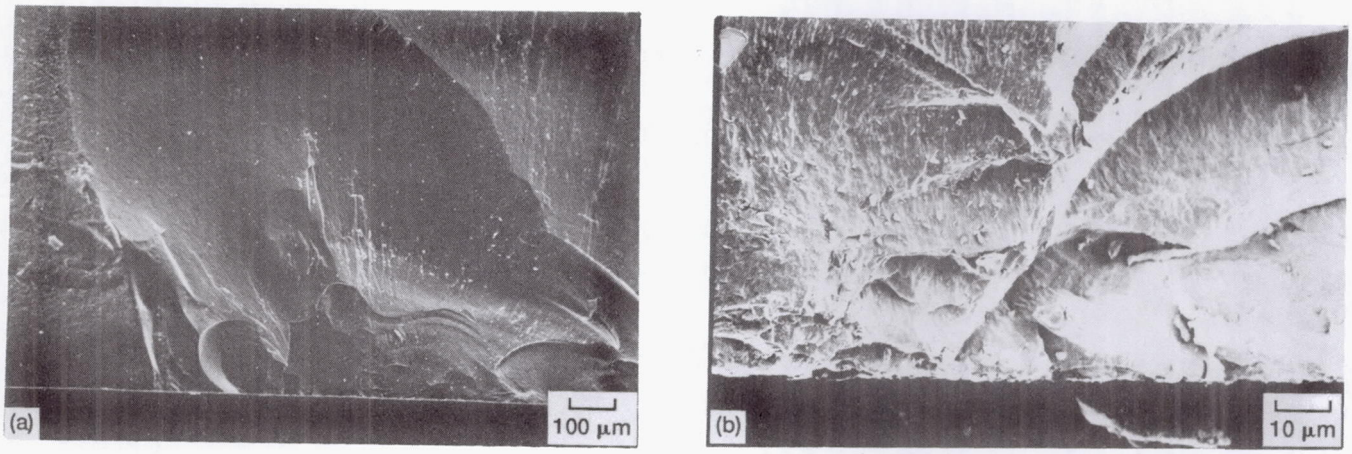

Figure 21.—SEM micrographs of fracture surface of LAS.

Local nonlinearities in monolithic ceramics and the presence of a definable relaxation strain are strategically important from a design perspective. This behavior indicates the potential for localized toughening mechanisms in ceramics and brittle matrices. Also, the reproducible relationship between the stresses implies a nonintrusive methodology for assessment of the reliability and strength of a material.

Strain Analysis of Monofilament Ceramic Composites

The SLAM strain measurements from the LAS/SiC monofilament composite specimens are given in Appendix H. These values represent the local strain induced within the ROI at predetermined subcritical stress levels. Relaxation strain (ϵ_r) observed upon unloading of the external stress is also noted for each specimen.

The LAS/SiC monofilament composites exhibited local stress-strain behavior similar to that described for the LAS monolithic test specimens (see Figure 22). The local stress-strain curves for each composite specimen exhibited a nonlinear component, and a measurable relaxation strain.

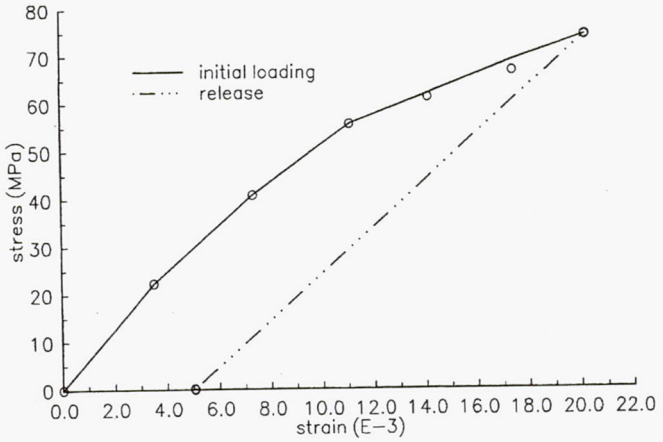

Figure 22.—Local stress-strain behavior for monofilament composite in four-point flexture.

The measured relaxation stresses, flexural strengths (fracture stress), and local yield stresses for each specimen tested in SLAM are tabulated in Table 7. The ratios of the relaxation to fracture stresses are also given for each LAS/SiC specimen. The ratios are correlated with the fracture mode of the specimen; specimens which failed by shear at the fiber-matrix interface are indicated by asterisks in the table and have ratios greater than 0.30.

Table 7: Experimental Local Yield, Relaxation, and Fracture Stresses for LAS/SiC Monofilament Composites

Specimen	Yield Stress (σ_y), MPa	Rel. Stress (σ_r), MPa	Frac. Stress (σ_f), MPa	Ratio (σ_r/σ_f)
1	47	27	111.2	0.242
2	45	15	91.8	0.163
3	40	17	104.9	0.162
4	47	28	114.2	0.245
5	40	38	106.8	0.356*
6	43	29	119.0	0.244
7	55	40	101.2	0.395*
8	39	34	104.9	0.324*
9	46	30	112.0	0.267
10	39	28	126.5	0.221
Mean/Sigma	44.1/5.0	28.6/8.0	109.2/9.6	.220/.042 .358/.034*

The mean measured flexural strength for the single fiber reinforced composites was 109.2 ± 9.6 MPa (statistically equivalent to the mean flexural strength of the LAS monolithics). The single fiber reinforcing the LAS matrix corresponds to a fiber volume fraction near zero ($V_f \sim 10^{-4}$) thereby allowing little strength enhancement, according to the rule of mixtures. However, the local yield of the stress-strain curves tended to occur at slightly lower stress levels than was found for the LAS monolithics (44 MPa for the composite in comparison to 55 MPa for the LAS monolithics). This suggested enhanced matrix microcrack propagation for the monofilament composites.

Fracture analysis of the fractured LAS/SiC monofilament test specimens indicated two distinct fracture modes. The bulk of the specimens failed due to multiple matrix cracking emanating from the tensile region of the test specimens. As with the monolithics, these specimens exhibited a significant amount of localized matrix cracking and microcracking off the primary crack path as well as localized sites for fracture initiation. Figure 23 shows SEM micrographs from the tensile zone of the matching fracture surfaces (Figure 23a) and the fractured fiber region (Figure 23b) for a LAS/SiC monofilament composite. The occurrence of multiple crack zone sites and extensive microcracking along the tensile surface is evident in Figure 23a. Figure 23b shows bonding at the fiber-matrix interface. Strong (chemical) bonding inhibits deflection of propagating cracks at the fiber-matrix interface.

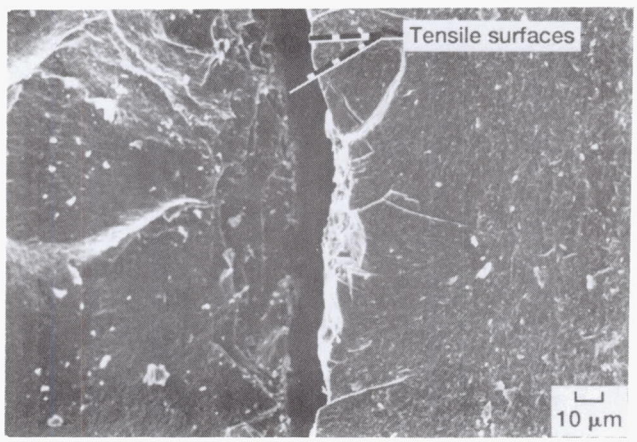

(a) Tensile surface region.

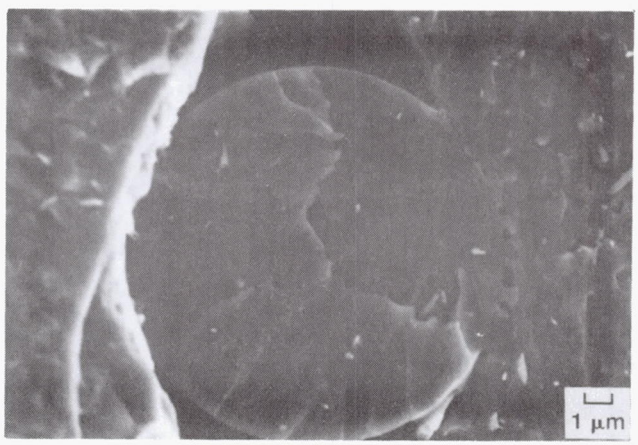

(b) Fiber-matrix interface region.

Figure 23.—SEM micrographs of fracture surfaces of monofilament composite.

Thirty percent of the test specimens failed due to shear along the fiber-matrix interface. SEM analysis of the fracture surfaces of these test specimens indicated that an inadequate bond was formed between the fiber and the matrix and the load was not effectively transferred from the matrix to the fiber. In these cases, the crack front emanating from the tensile side of the bar was permitted to advance past the fiber toward the compressive region. The SEM micrograph in Figure 24 shows that the crack front propagated from the fiber-matrix interfacial region toward the compressive zone. The void population present in the interfacial region is indicative of poor bonding (debonding) at the interface.

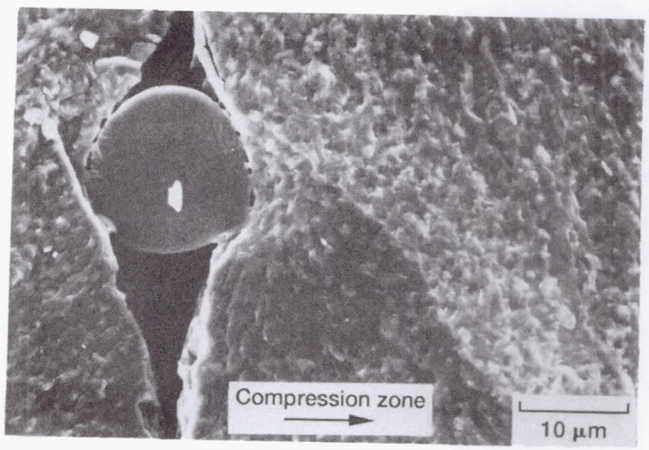

Figure 24.—Crack advancing through fiber in poorly bonded composite.

The weakest link in a composite system is frequently the bond formed at the matrix-fiber interface. This was particularly true for the monofilament composite specimens used in this study due to the processing procedure employed. In cases

where there was poor bonding at the interface, significant shear stresses could be built up at relatively low loading levels.

Analysis of the relaxation strain (stress) induced due to mechanical loading and unloading indicated that there was a definable quantitative relationship between the fracture stress and the relaxation stress for each specimen. However, for the monofilament reinforced LAS, there was a bimodal distribution in the ratio between the relaxation stresses and the fracture stresses, with the bifurcation predicated on the dominant fracture mode of the test specimen (see Table 7). This indicated a relationship between the relaxation stresses (strains) and the local microstructural anomalies of the test specimens.

For the specimens which failed due to cracking on the tensile side of the bar, the ratio of the relaxation to fracture stress was 22.0 ± 4.0 percent. This ratio is slightly higher than was determined for the LAS monolithic test specimens (18.5 percent), though still within the experimental uncertainty of the measurement.

For the specimens which failed due to shearing at the fiber-matrix interface, the ratio was 35.8 ± 3.5 percent. This relatively high ratio indicated that matrix stress relaxation occurred at higher stresses (approximately 38 MPa) than was observed in the monolithics. It is likely that the applied loads were sustained as shear stresses at the weak fiber-matrix interface before the characteristic multiple matrix microcracks

for stress relief were generated. The higher ratio may be attributed to these shear stresses at the fiber-matrix interface.

The SLAM interferograms resulting from the LAS/SiC monofilament composites had a considerably lower SNR than was observed for the LAS monolithic materials (see Figure 25). The degraded SNR was primarily attributed to grinding marks on the surface of the processed composite specimens. Though the low SNR made measurability of the strain more difficult, the data does indicate that the test measurement technique was not overly sensitive to surface finish.

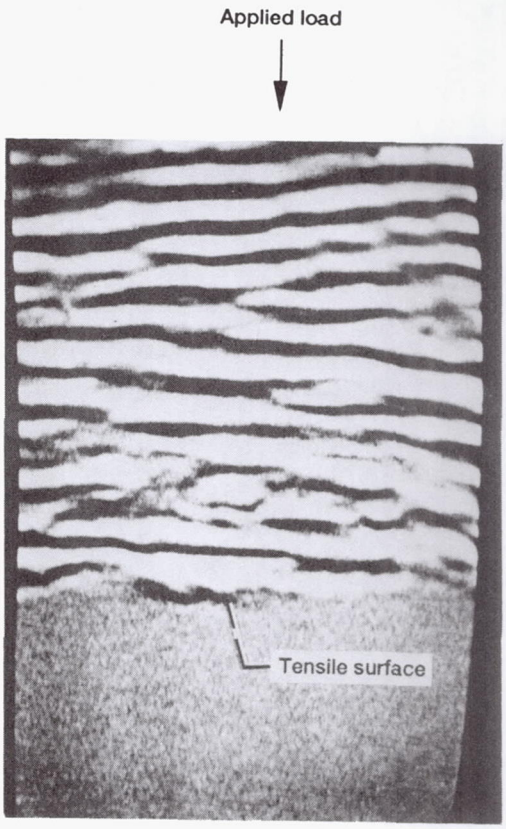

Figure 25.—Interference fringes from LAS/SiC monofilament composite.

Strain Analysis of Ceramic Composites

The unprocessed SLAM strain measurements for the Corning calcium alumino-silicate/Nicalon SiC composite specimens are given in Appendix I. The local strain measurements at the predetermined stress levels and relaxation strains for each specimen are indicated. Figure 26 depicts the typically observed local stress-strain behavior of the CAS/SiC composite. In this case, the observed nonlinear mechanical behavior effects conform with the behavior typically reported for composites. Composites exhibit multiple matrix fracture and interface debonding prior to final failure. These composites are therefore not linearly elastic to failure [89,90]. This general behavior was also observed in the load-deflection curves recorded during flexural strength testing and is reported in the literature [91].

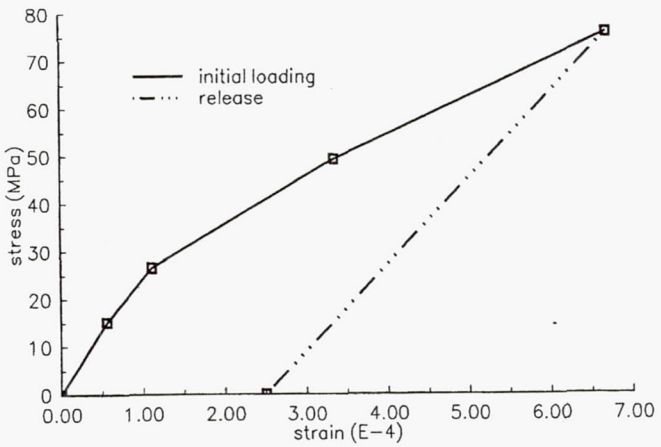

Figure 26.—Local stress-strain behavior of CAS/SiC in four-point flexure.

Table 8 presents the measured relaxation, yield, and ultimate stress data for the CAS/SiC specimens investigated. The ratios between the experimentally determined relaxation stresses and yield stresses for each specimen are also given.

Most researchers consider the onset of nonlinearity in the load deflection curve to correspond to the initiation of matrix cracking. As shown in Table 8, the mean yield stress for the CAS/SiC composites occurred at 419 ± 33 MPa (55.2 ± 4.8 ksi). However, analysis of the stress-strain curves, generated from localized SLAM strain measurements within the tensile zone, indicated that the deviation from linearity occurred at significantly lower stress levels. The mean local yield stress for the CAS/SiC specimens was 36 MPa. This behavior follows the trend discussed in the previous sections. With a typical volume fraction of 35 percent for CAS/SiC composites, the presence of the reinforcing fibers strengthens the matrix, according to the rule of mixtures, but also promotes matrix microcracking. Thus, matrix damage can occur at lower stress levels.

It was previously shown that local microcracking in monolithic ceramics was not a prerequisite for nonlinearity in load deflection curves. This suggests that the initiation of matrix microcracking in ceramic composites may actually occur prior to nonlinearity.

Comparison of the measured local relaxation stress to the yield stress for each composite specimen produced a quantitative relationship similar to that described for

Table 8: Experimental Relaxation, Yield, and Ultimate Stresses for CAS/SiC Composite

Spec.	Loc. Yield (σ_l), MPa	Rel. Str. (σ_r), MPa	Yield (σ_y), MPa	Ult. Str. (σ_u), MPa	Ratio (σ_r/σ_y)
1	40	49.3	417.2	826.8	.118
2	40	48.4	439.9	826.8	.110
3	40	49.3	493.0	804.0	.100
4	45	49.3	417.2	849.5	.118
5	36	55.9	424.8	1047.0	.131
6	26	37.9	379.3	804.0	.100
7	38	33.1	402.0	879.9	.082
8	39	45.5	379.3	876.1	.120
Mean± Sig.	36.3±5.4	46.1±7.2	419.0±37	864.3±79	.110± .015

the previous material systems. The ratio of the relaxation stress to the yield stress was 11.3 ± 1.1 percent for the CAS composites. As with the LAS monolithics, there appeared to be a definitive correlation between relaxation stresses initiated by microcracking and the failure of the matrix. There was no apparent correlation between the measured relaxation stress and the ultimate failure stress of the composite since the ultimate stress was primarily dependent upon the fiber, not the matrix, behavior.

The experimentally determined stress relaxation ratio for the CAS/SiC composites was significantly smaller than the ratio determined for either the LAS monolithics or the LAS/SiC monofilament composites. The change in matrix material from LAS to CAS may explain the lower measured ratio.

The coefficient of thermal expansion mismatch in the CAS/SiC composite material leads to the development of residual tensile stresses in the CAS matrix during processing [47]. These stresses would contribute to the evolution of matrix microcracking for stress relief. In contrast, the coefficient of thermal expansion mismatch in the LAS/SiC composite material leads to internal compressive stresses in the matrix [11] which must be overcome by the applied loads, in order for matrix microcracks to propagate. In this case, the anisotropy of the coefficient of thermal expansion within the matrix material provides the dominant residual stress effect available for relief. However, compressive residual stresses in the matrix tend to inhibit the stress relaxation and higher applied stresses are required to initiate stress relief.

The CAS/SiC composites were reinforced with Nicalon SiC fibers which were previously shown to exhibit large variances in elastic modulus. These variations affect the mechanical properties at the local level in the composite system. Local regions of the composite which are reinforced with low modulus fibers are less susceptible to fiber pullout as external stresses are applied since the resistive frictional force at

the fiber-matrix interface is increased [39]. At the same time, the localized regions containing the low modulus fibers experience matrix cracking at lower stress levels than regions reinforced with high modulus fibers. This corresponds to local yielding at lower applied stress levels.

The microcracking and ultimate failure process for the CAS/SiC composites was much more complex than was observed with either the monolithic or monofilament composite test specimens. For the CAS/SiC composites investigated, the dominant cracks were initiated on the tensile side of the beam and propagated to approximately midplane. Final failure tended to occur by shear fracture along the midplane of the beam. Figure 27 shows optical micrographs of the fracture path through the CAS/SiC specimens. This failure mechanism has been shown to predominate in composites loaded in four-point flexure where the ratio of the separation of the major and minor spans to the thickness of the flexural beam is small (less than 5) [39]. For the experimental configuration used in the present work, this ratio was approximately 4.8 for the CAS/SiC test specimens. SEM micrographs of the ROI of the fractured CAS/SiC test specimens (Figure 28) showed that there was extensive fiber pullout throughout the tensile zone and increased fiber damage along the region of shear failure. The occurrence of fiber pullout is likely to account, in part, for the presence of macroscopic nonlinearities in the mechanical behavior. In addition, multiple matrix microcracks propagated off the primary crack path. This

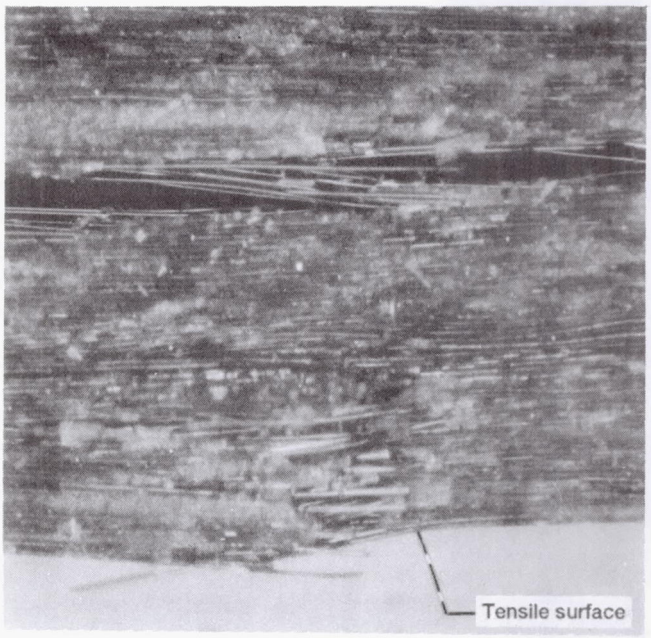

Figure 27.—CAS/SiC composite after fracture in four-point flexure.

accounted for the observed local nonlinearities. It is important to point out that the accumulation of matrix damage throughout the tensile zone destroyed the uniformity of the beam and calculations of stresses based on linear elastic beam theory were not necessarily valid.

The Aveston et al. (ACK) and Marshall et al. (MCE) models for matrix cracking in composites are often used to predict the stress at which permanent damage occurs in the matrix of composite materials (see Appendix A). The first matrix cracking stress for the CAS/SiC composites, based on the ACK model described in Appendix A, was 376 MPa. As previously discussed, the onset of nonlinearity in the experimental load deflection curves has been widely accepted to be the first matrix cracking stress. Indeed, the experimentally determined yield stress compares very well (within 1.3 percent) to the first matrix cracking stress predicted

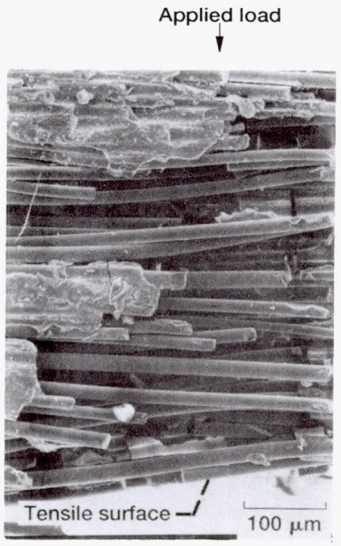

Figure 28.—SEM micrograph showing fiber pullout of CAS/SiC composite.

by the ACK model. However, the observed local stress-strain behavior for CAS/SiC indicated that the ACK model overpredicts the stress for first matrix cracking.

Both the ACK and MCE models assume that the first matrix cracking stress corresponds to the initiation of steady state cracking, i.e. the state at which the crack length no longer affects the stress intensity. However, the present study indicates that matrix cracking occurs in the glass ceramic based materials prior to the initiation of steady state cracks which dominate the matrix. Instead, first matrix cracking corresponds to the initiation of localized microcracking which gives rise to local mechanical hysteresis. The observed macroscopic nonlinearity of load-deflection test curves cannot be used to determine the onset of matrix cracking but, instead, is likely to correspond to the domination of matrix damage due to multiple matrix cracks.

Recently, researchers at the University of Dayton Research Institute have reported similar findings on CAS/SiC test specimens loaded in tension [47]. As the specimen was loaded, acoustic emission was used to detect the stress at which matrix cracking initiated. In all cases, the acoustic emission studies detected the occurrence of first matrix cracking prior to the onset of nonlinearity in the load deflection curves. However, a direct one-to-one comparison with the present data cannot be made since these experiments were macrocrack studies conducted under tensile loading conditions. The loading condition, as well as the crack size, environment, material, and processing parameters will effect the nature of the fracture mechanisms and observed mechanical behavior of the specimens.

Discussion

The strain measurements made using the SLAM measurement model were directly dependent upon the accuracy of the velocity of ultrasonic wave propagation through the material and the magnitude of the strain-optic coefficients. Measurement of the velocity of sound by cross correlation was chosen for this study because it provided the most accurate experimental determination of the wave velocity [69]. However, potential errors in the measured velocity arose from thickness variations across the test specimen, thickness variations of the fluid couplant used in the test setup, time base precision, diffraction phase shift, dispersion effects and attenuation [92].

Previous researchers have estimated the measurement uncertainty based on these considerations to be less than 0.36 percent [93].

True measurement quantification requires calibration to a verifiable standard. Two essential characteristics of a reliable calibration standard are permanence and reproduceability [94]. However, reliable acousto-optical standards are difficult to obtain [95]. Anomalies within a material's structure which occur during processing alter the acousto-optical response of the material. This degrades the relevance of the standard to a particular test specimen and challenges the validity of the measurement made with respect to such a standard.

The strain measurements reported in this investigation were made with respect to the acousto-optical response produced at an initial (zero) stress level on the as-received specimens. The as-received state of the material was used as a reference condition. In this way, the lack of reliable acoustic standards for these measurements was circumvented by allowing each test specimen to function as its own standard. This practice can provide reliable induced strain measurements but cannot be used as a method for measuring the absolute strain of the material, vis-a-vis measurements inclusive of internal strains inherent to the material. When reliable acoustic and/or acousto-optical standards become available, it is recommended that all strain measurements be appropriately calibrated.

It is, however, important to point out that the conclusions determined regarding the relaxation stresses and resulting correlation to the destructive testing results provide unique and valid information regarding the onset of matrix microcracking and damage in both the monolithic and composite test specimens.

CHAPTER VI

SUMMARY AND CONCLUSIONS

This research effort has included an analysis of the effects of externally applied loading on the mechanical behavior of the individual constituents of a glass ceramic composite and the total composite system. As a consequence of this work, it has been shown that the scanning laser acoustic microscope (SLAM) provided high resolution capability for quantitatively analyzing the mechanical behavior of materials for which reliable empirical investigation was previously not possible. This included the analysis of small diameter ceramic fibers and a study of localized mechanical behavior of monolithics ceramics and ceramic composites. The utilization of a high resolution acousto-optical measurement methodology (SLAM) has provided simultaneous qualitative and quantitative characterization of the in situ local stress-strain behavior of silicon carbide fiber, a glass ceramic, and a silicon carbide reinforced glass ceramic composite.

The principal ramifications of the results obtained were

1. A definitive technology for the strain measurement and mechanical characterization of ceramic monofilaments now exists and can be utilized for the investigation of future ceramic fibers as the process is refined and test specimens become available.

2. The fiber analysis has quantitatively described the influence of local microstructural variations on the observed elastic modulus and provided a quantitative basis for characterization of composite structures.

3. A reliable technology for the analysis of the local mechanical behavior of ceramics and ceramic composites is defined and can be used to monitor the progression of microcrack initiation and propagation on a local level in brittle materials. This aids in our understanding of crack evolution and will play an important role in the improvement of ceramics for structural applications.

4. The analysis of the monolithics has indicated that local nonlinearity in the mechanical behavior occurs, resulting in a definitive threshold for microcrack initiation. The threshold correlates with the fracture behavior of the test specimen and is related to the inherent residual stress in the test specimen and the influence of the crack front with local microstructural variations. A mechanism for local toughening which can be exploited for enhanced performance is implied.

5. The analysis of simple composites, i.e., single fiber reinforced specimens, has indicated that local relaxation stress and the relationship to the fracture behavior of the composite can serve as indicators of relative interfacial bond strength. This assessment is critical to the development and characterization of reliable composite structures.

Discussion

Modifications in the analysis of the SLAM response provided the capability for measuring the tensile strain of small diameter (to 15 μm) ceramic fibers. The Nicalon silicon carbide (SiC) fibers studied in this investigation exhibited widely varying mechanical behavior responses to externally applied tensile stresses, indicating significant macrostructural and microstructural variations from specimen to specimen. There were also significant variations (20 percent) in the diameter of the fibers. These variations and microstructural anomalies due to processing alter the fracture behavior of the specimens.

The mean elastic modulus of the Nicalon SiC fiber determined by analysis of the linear regression of the experimental stress-strain curves (185.3 GPa) compared favorably with values reported in the literature. A statistical analysis of the elastic modulus data for fifteen independent test specimens showed that the variations in the elastic modulus were due to real microstructural variations in the fibers while

variations in the measurement due to random measurement deviation was limited to 2.6 GPa.

The mechanical behavior of a composite material is dependent upon the elastic modulus of the matrix and fiber, according to the rule of mixtures. The wide variance in the elastic modulus for individual Nicalon SiC fibers implies that there may be corresponding localized regions exhibiting relatively poor elastic properties within a composite structure reinforced with these materials. The application of SLAM to analysis of small diameter fibers provides an avenue for in-line quality control and feedback to processing. Ultimately, this would provide composite structures with enhanced performance and reliability.

Measurement of the in situ local strain behavior of lithium alumino-silicate (LAS) monolithic glass ceramic showed that the material tends to exhibit nonlinear mechanical behavior and relaxation effects due to external loading. The nonlinear effects were interpreted as localized microcracking due to internal stress in the LAS. The SLAM measurement data showed that stress relaxation occurred repeatably at a mean value of 18.5 percent of the fracture stress for each LAS specimen studied, signifying a definitive measure of the internal residual stress for this material system. The stress relaxation ratio was a material characteristic dependent upon the fracture properties of the system.

The fracture analyses of the LAS monolithic specimens also indicated marked sites of local crack initiation and microcracking deviating from the primary crack path. The presence of multiple crack sites in a monolithic ceramic material indicates that the mechanical behavior at a localized level deviates significantly from the global mechanical behavior typically used for design analysis. In fact, we can infer a definitive threshold for microcrack initiation and propagation.

A further ramification of the localized nonlinear behavior is the occurrence of localized toughening in ceramic structures. This suggests that the cracking phenomena in monolithic brittle materials is not as straight forward as is implied by elasticity theory. In fact, local cracking behavior in monolithic ceramics is a complex process. A thorough understanding of the local crack evolution may allow exploitation of the small crack regime for ceramic toughening.

A single fiber embedded in a glass ceramic matrix has a small but measurable effect upon the observed stress at which matrix microcracking occurs when there is sufficient bonding at the fiber-matrix interface. However, frictional effects between the single fiber and the matrix are not sufficient to dominate the micromechanical behavior. Weak bonds between the fiber and the matrix offer little resistance to propagating cracks but allow the applied load to be effectively transferred primarily to shear stresses at the interface. Domination of the shear stresses allows little load transfer to the matrix and a significantly higher stress for matrix stress relaxation

results. The relative stress for microcracking to the fracture stress was shown to relate to the dominant fracture mode of the material.

Observed macroscopic nonlinearities in the mechanical behavior of composite specimens were shown to be due to domination of matrix damage by steady state cracking rather than the onset of matrix cracking. The onset of matrix cracking and the development of steady state crack propagation are not necessarily coincident. The Aveston et al. (ACK) model and Marshall et al. (MCE) model for predicting the matrix cracking stress are often used to also predict the onset of mechanical nonlinearity. This interpretation of the models assumes that steady state crack propagation has occurred. However, local analyses indicate that the stress for first matrix cracking is overpredicted.

The analysis of the in situ local mechanical behavior provided a unique insight into the effect of the micromechanical behavior of the fiber-matrix interface on the total composite behavior. Further, microstructural mechanical analyses allow projections of the observed mechanical behavior to be interpreted in terms of the microstructural domain.

The crack evolution within the composite structure is a complex process which includes the effects of friction at the fiber-matrix interface, the stress required for relaxation of internal residual stresses, and local microstructural interactions. First matrix cracking stress in composites is often considered to be an important parameter

for these materials. However, the complex nature of the crack process implies that true first matrix cracking occurs at relatively low load levels characteristic of the residual effects of the composite.

Local analysis of monolithic and more complex ceramic systems allows a unique opportunity for advancement of insight into the crack evolution process. Implementation of scanning laser acoustic microscopy provides an opportunity for the high resolution nonintrusive investigation of crack evolution and its relationship to stress relaxation as well as empirical fiber characterization. This information is necessary to process improved composite structures with enhanced reliability.

CHAPTER VII

RECOMMENDATIONS FOR FUTURE WORK

The work presented in this research effort clearly indicates the need for enhanced analysis of both monolithic and composite material systems at the local and microstructural level. Interpretation of the experimental results in terms of the fracture parameters and properties is a necessary step in the design and implementation of composite systems for structural applications.

The evolution of the crack process which leads to local nonlinear behavior must be more fully understood in order for local toughening to be effectively exploited for potential design applications. In this work, the relaxation strain was measured by unloading the specimen directly from the maximum applied load to the initial stress state. A more comprehensive interpretation of the stress relaxation and crack behavior may be gained by incremental unloading. This allows the form of the unloading curve to be determined and yields information regarding crack closure effects.

Cycling of the applied stress and incremental measurement of the local strains produced will also enhance the existing information on the evolution of the crack. This will also provide insight into the effect the local microcracking has upon the general material behavior. In addition, in this work only three LAS specimens were studied for their measured stress relaxation as a function of the applied stress prior to unloading, due to the limited availability of test specimens. A more statistically sound approach to this analysis will provide a more reliable data base. In addition, the composite specimens should be analyzed in an analogous way. Local mechanical behavior of a particular material is likely to be strongly dependent upon the hysteresis effects of the material and any memory that the material may have. This must be assessed for each material system on an individual basis.

It has been speculated from this work that there is a measurable threshold stress for microcrack initiation and propagation. A definitive comparison of the relationship between the stress relaxation ratio and the ratio of the stress intensity threshold to the fracture toughness of the material should be completed. One might infer that the stress intensity ratio and the stress relaxation ratio describe analogous behavior. A statistical experiment measuring the stress relaxation ratio and the stress intensity threshold ratio should be conducted.

The mechanical behavior response of a material class may be affected by the loading conditions, loading rate, and environmental conditions. In order to

effectively select a material for a particular application, it is critical to assess the behavior of the material system as a function of these operating parameters. Since the SLAM system methodology exploited for this work incorporates the in situ analysis of materials, it potentially lends itself to the materials analysis under a variety of loading conditions. Most of the analyses described in this work were performed under tensile (fibers) or four-point flexural (composites) loading. It would be useful to perform the materials analyses under loading conditions more representative of those used in actual operation.

Only a single composite system was studied in detail in this investigation. However, there are a number of candidate systems for potential elevated temperature structural applications. The in situ mechanical behavior of other systems such as the silicon carbides, silicon nitrides, and derivatives thereof may prove to be critical from a structural design perspective. Since the local mechanical behavior of the glass ceramics exhibited nonlinearities, it is important to investigate this level in the structural design candidate materials as well.

From a measurement methodology perspective, it is important to develop the data acquisition and analysis equipment to provide a measurement strategy for materials under their operating conditions. This requires an adaptation of the existing measurement equipment to provide the in situ analysis of materials at elevated temperatures. For the material systems of interest in elevated temperature

structural applications, the characterization strategy must provide capability for measurement at temperatures to 1400°C. In the case of the existing SLAM system, this will require the development of an apparatus for specimen heating to the required temperature, assessment of the temperature along the specimen zone, maintenance of the thermal integrity of the zone surrounding the specimen, and development of effective acoustic wave transfer to the specimen capable of withstanding the elevated temperature environment without altering the test specimen.

The existing measurement system also does not presently provide an automated measurement capability. A skilled operator is required to measure the fringe shift. The measured shifts are manually recorded and a computer program was written to determine the strain measurements. Automation of this measurement procedure will optimize the efficiency and validity of the measurement.

The measurement of the elastic modulus of ceramic whiskers is another important step in optimizing the ceramic composites used for structural components. Since the SLAM measurement system does not require long gauge length or large diameter specimens for analysis, it lends itself easily to the in situ strain measurement of ceramic whiskers.

REFERENCES

[1] Griffith, A.A., *Philos. Trans. R. Soc.*, A221(4), 163 (1920).

[2] Bourne, G.H. ed., *The Biochemistry and Physiology of Bone*, London: Academic Press Inc., (1972).

[3] Ashby, M.F. and Jones, D.R.H., *Engineering Materials 2: An Introduction to Microstructures, Processing and Design*, New York: Pergamon Press, (1986).

[4] Brooks, A., Morgan, W., Lissaman, P., MacCready, P., "Development of a Wing Flapping Flying Replica of a Pterosaur", *AIAA* 85-1446, Washington D.C. (1985).

[5] Pride, R.A., "NASA Flight Service Programs to Evaluate Composite Structural Components", *18th Natl. SAMPE Symp. Exhib.*, Los Angeles, CA, (1973).

[6] August, A., Hadcock R., and Dastin, S., "Composite Materials Design from a Materials and Design Perspective", *AGARD Rep.* 639, (January 1976).

[7] Meade, L.E., "DOD/NASA Structural Composites Fabrication Guide", 2nd ed., vol.1, secs. 1 to 9-60, AFWAL, Wright Patterson AFB, Dayton, OH and Lockheed-Georgia Co., Marietta, GA, F33615-77-C-5256, (May 1976).

[8] Salkind, M.J., "Aerospace Materials Research Opportunities", *Angew. Chem. Adv. Mater.* 101 (5), 671 (1989).

[9] Zweben, C., "Advanced Composites: A Revolution for the Designer", *AIAA* 81-0894, Long Beach, CA, (May 1981).

[10] Schwartz, M.M., *Composite Materials Handbook*, New York: McGraw-Hill Book Co., (1985).

[11] McMillan, P.W., *Glass Ceramics*, 2nd ed., New York: Academic Press, (1979).

[12] Prewo, K.M., and Brennan, J.J., "High-strength Silicon Carbide Fibre-reinforced Glass-matrix Composites", *J. of Mat. Sci.*, 15, 463-8 (1980).

[13] Thompson, E.R., "Composite Material Systems for High Temperature Applications", *AGARD Conf. Proc.*, (1989).

[14] *Net Shape Technology in Aerospace Structures*, Washington D.C.: National Academy of Science Press, (1986).

[15] Covault, C., *Aviat. Week Space Technol.*, 36, March 7, 1986.

[16] Hadcock, R., "Status and Viability of Composite Materials in Structures of High Performance Aircraft", National Research Council, Aeronautics and Space Engineering Board, Naval Postgraduate School, Monterey, CA (1986).

[17] Ronald, T., "Structural Materials for NASP", *AIAA Third Internat. Aerospace Planes Conf.*, 91-5101, Orlando, FL (1991).

[18] Brown, A., "Materials Pace ATF Design", *Aerosp. Am.* 25 (4), 16-22, (1987).

[19] United States Congress, Office of Technology Assessment, "New Structural Materials Technologies", (1986).

[20] Henderson, R. and Petty, J., "Advanced Technologies for Aero Gas Turbine Components", *AGARD Conf. Proc.* 421 (1987).

[21] Prewo, K.M., Johnson, B., Starrett, S., "Silicon Carbide Fibre-reinforced Glass-ceramic Composite Tensile Behaviour at Elevated Temperature", *J. of Mat. Sci.*, 24, 1373-9 (1989).

[22] DiCarlo, J.A., "High Temperature Structural Fibers: Status and Needs", *NASA TM 105174* (1991).

[23] Sokolov, S., USSR Patent No. 49 (August 31, 1936), British Patent No. 477 139, 1937, and U.S. Patent No. 21 64 125, 1939.

[24] Dunn, F. and Fry, W.J., "Ultrasonic Absorption Microscope", *J. Acoust. Soc. Am.*, 31 (5), 632-33, (1959).

[25] Lemons, R.A. and Quate, C.F., "Acoustic Microscope--Scanning Version", *Appl. Phys. Letters*, 24 (4), 163-5, (1974).

[26] Korpel, A. and Desmares, P., "Rapid Sampling of Acoustic Holograms by Laser-Scanning Techniques", *J. Acoust. Soc. Am.*, 445 (4), 881-4 (1969).

[27] "Standard Test Method for Tensile Strength and Young's Modulus for High-Modulus Single-Filament Materials", *Annual Book of ASTM Standards: General Products, Chemical Specialties, and End Use Products*, High Modulus Fibers and Composites, Sect. 15, Vol. 15.03, D3379-75 Philadelphia, PA: American Society for Testing and Materials, (1991).

[28] DiCarlo, J.A., NASA Lewis Research Center, Cleveland, OH (1991), personal communication.

[29] Cook, R.F., Lawn, B.R., and Fairbanks, C.J., "Microstructure Strength Properties in Ceramics: I, Effect of Crack Size on Toughness", *J. Am. Ceram. Soc.*, 68 (11), 604-15 (1985).

[30] Whitman, R.L. and Korpel, A., Probing of Acoustic Surface Perturbations by Coherent Light, *Appl. Optics*, 8 (8), 1567-76 (1969).

[31] Prewo, K.M., "The Chemical Processing of Structural Ceramics for Use in Severe Environments Workshop", U.S. Air Force Office of Scientific Research (1984).

[32] Kingery, W.D., Bowen, H.K., and Uhlmann, D.R., *Introduction to Ceramics*, 2nd ed., New York: John Wiley & Sons, Inc., (1976).

[33] Brennan, J.J. and Prewo, K.M., *J. of Mat. Sci.*, 17, 2371 (1982).

[34] Prewo, K.M., "Ceramic-Ceramic Composites", notes from presentation, (1984).

[35] Jamet, J.F., Lewis, D., and Luh, E.Y., "Characterization of Mechanical Behavior and Fractographic Observations on Compglas SiC/LAS Coposites", *Ceram. Eng. and Sci. Proc.*, 5, 625 (1984).

[36] Sokolnikoff, I.S., *Mathematical Theory of Elasticity*, 2nd ed., New York: McGraw-Hill Book Co. Inc., (1956).

[37] Whitney, J.M., "Analytical Mechanics of Composites", MAT 543, University of Dayton, Dayton, OH, (1990).

[38] Richerson, D.W., *Modern Ceramic Engineering: Properties, Processing, and Use in Design*, New York: Marcel Dekker Inc., (1982).

[39] Marshall, D.B. and Evans, A.G., "Failure Mechanisms in Ceramic-Fiber/Ceramic-Matrix Composites", *J. of the Am. Ceram. Soc.,* 68 (5), 225 (1985).

[40] Coyle, T.W., Fuller Jr., E.R., Swanson, P., Palamides, T., "Fracture Mechanics Characterization of Crack/Fiber Interactions in Ceramic Matrix Composites", *Ceram. Eng. Sci. Proc.*, 8 (7-8), 630 (1985).

[41] Mah, T., Mediratta, M.G., Katz, A.P., Ruh, R., Mazdiyasni, K.S., "Room Temperature Mechanical Behavior of Fiber-Reinforced Ceramic-Matrix Composites", *J. of the Am. Ceram. Soc.*, 68 (1), C-27 (1985).

[42] Prewo, K.M., Johnson, B., Starrett, S., " Silicon Carbide Fibre-Reinforced Glass-Ceramic Composite Tensile Behaviour at Elevated Temperature", *J. of Mat. Sci.*, 24, 1373 (1989).

[43] Aveston, J., Cooper, G.A., Kelly, A., *Properties of Fiber Composites: Proc. of the Conference*, 15, England: IPC Science and Technology Press, Ltd., (1971).

[44] Marshall, D.B., Cox, B.N., and Evans, A.G., "The Mechanics of Matrix Cracking in Brittle-Matrix Fiber Composites", *Acta. Metall.*, 33 (11), 2013 (1985).

[45] Chulya, A., Gyekenyesi, J.P., Bhatt, R.T., "Mechanical Behavior of Fiber Reinforced SiC/RBSN Ceramic Matrix Composites: Theory and Experiment", *NASA TM 103688* (1991).

[46] Kim, R.Y. and Pagano, N.J., "Crack Initiation in Unidirectional Brittle-Matrix Composites", *J. Am. Ceram. Soc.*, 74 (5), 1082-90 (1991).

[47] Kim, R.Y., "Experimental Observation of Progressive Damage in SiC/Glass-Ceramic Composites", to be published in *Ceram. Eng. and Sci. Proc.*, American Ceramic Society 16th Annual Conference on Composites and Advanced Ceramics, Cocoa Beach, FL (1992).

[48] Kessler, L.W., Palermo, P.R., and Korpel, A., "Acoustic Microscopy", *Nature*, 232, 110, (1971).

[49] Yuhas, D.E. and Kessler, L.W., *Acoustical Imaging: Visualization & Characterization* ed. K Y. Wang, Vol. 9, New York: Plenum Press, (1980).

[50] Kessler, L.W. and Yuhas, D.E., "Acoustic Microscopy-1979", *Proc. of the IEEE*, 67 (4), 526 (1979).

[51] Love, G.R. and Ewell, G.J., "Acoustic Microscopy of Ceramic Capacitors", *IEEE Transactions* CHMT-1 (3) (1978).

[52] Kessler, L.W. and Yuhas, D.E., "Listen to Structural Differences", *Industrial Research/Development* (April 1978).

[53] Kessler, L.W. and Yuhas, D.E., "Structural Perspective", *Industrial Research* (Jan. 1978).

[54] Oishi, M., Hoguchi, K., Masaki, T., and Mizushina, M., "Measurement of Elastic Constants of Ceramics by a Scanning Laser Acoustic Microscope", *MRS Inter. Meeting on Adv. Mat.* Vol.5, 93 (1989).

[55] Roth, D.J., Generazio, E.R., and Baaklini, G.Y., "Quantitative Void Characterization in Structural Ceramics Using Scanning Laser Acoustic Microscopy", *NASA TM 88797* (1986).

[56] Generazio, E.R. and Roth, D.J., "Quantitative Flaw Characterization with Scanning Laser Acoustic Microscopy", *Analytical Ultrasonics in Mat. Research and Testing Conf.*, NASA Lewis, Cleveland, OH (1984).

[57] Gottlieb, M., Ireland, C.L.M., and Ley, J.M., *Electro-optic and Acousto-optic Scanning and Deflection*, New York: Marcel Dekker, Inc., (1983).

[58] Kent, R.M and Vary, A., "Tensile Strain Measurements of Ceramic Fibers using Scanning Laser Acoustic Microscopy", to be published in *Cer. Eng. and Sci. Proc.*, American Ceramic Society 16th Annual Conference on Composites and Advanced Materials, Cocoa Beach, FL (1992).

[59] Kent, R.M. and Vary, A., "Strain Analysis of Ceramic Fibers using Scanning Laser Acoustic Microscopy", *Proc. 4th Annual HITEMP Review*, Cleveland, OH (1991).

[60] Goodman, J.W., *Introduction to Fourier Optics*, New York: McGraw-Hill Book Co., (1968).

[61] Hecht, N.L. and McCullum, D.E., "Characterization Studies of Ceramic Fibers", Dayton, OH: final report to System Research Labs (1984).

[62] Prewo, K.M., "Silicon Carbide Yarn Stimulates Development of New Composites", *Composites Review* Vol. 5, 69-71 (1983).

[63] Dow Corning Corp., specification data sheet, Midland, Michigan (1989).

[64] Yajima, S., "Development of Ceramics, Especially Silicon Carbide Fibers, from Organosilicon Polymers by Heat Treatment", *Phil. Trans. Roy. Soc.*, A294, 419-26, (1980).

[65] Roth, D.J., Stang, D.B., Swickard, S.M., and DeGuire, M.R., "Review and Statistical Analysis of the Ultrasonic Velocity Method for Estimating the Porosity Fraction in Polycrystalline Materials", *NASA TM 102501* (1990).

[66] Dixon, R.W., "Photoelastic Properties of Selected Materials and Their Relevance for Applications to Acoustic Light Modulators and Scanners", *J. Appl. Physics*, 38 (13), 5149-53 (1967).

[67] Powell, J.A., "Refractive Index and Birefringence of 2H Silicon Carbide", *NASA TN D-6635* (1972).

[68] Breazeale, M.A., Contrell Jr., J.H., and Heymann, J.S., "Ultrasonic Wave Velocity and Attenuation Measurements", *Methods of Experimental Physics, Ultrasonics*, ed. P.D. Edmonds, Vol. 19, London: Academic Press, (1981).

[69] Hull, D.R., Kautz, H.E., and Vary, A., "Measurements of Ultrasonic Velocity using Phase-Slope and Cross-Correlation Methods", *Mater. Eval.*, 43, 1455-60 (1985).

[70] Papadakis, E.P., "Ultrasonic Diffraction from Single-Apertures with Application to Pulse Measurements and Crystal Physics, *Physical Acoustics*, eds. W.P. Mason and R.N. Thurston eds., Vol. XI, London: Academic Press, 152-211 (1975).

[71] Lempriere, B.M., "Standardizing Ultrasonic Attenuation Measurements" *Proc. JANNAF*, CPIA publ. 514 (1989).

[72] Krautkramer, J. and Krautkramer, H., *Ultrasonic Testing of Materials*, 4th ed., New York: Springer-Verlag, (1990).

[73] May, J.E., "Precise Measurement of Time Delay", *IRE Natl. Conv. Rec.*, 6:Part 2, 134-42 (1958).

[74] Corning Glass Works, *Glass-Ceramic Matrix Composite Research*

[75] Yajima, S., et al., "Elevated Temperature Strength of Continuous SiC Fibers", *Bulletin Am. Cer. Soc.*, 55, 1065, (1976).

[76] Hurwitz, F., NASA Lewis Research Center, Cleveland, OH, (1991), personal communication.

[77] DiCarlo, J.A., NASA Lewis Research Center, Cleveland, OH, (1991), personal communication.

[78] Dept. of the Army, "Flexural Strength of High Performance Ceramics at Ambient Temperature", *Mil. Stand. 1942A*, (1983).

[79] Brennan, J.J., United Technologies Research Center, East Hartford, CT, (1991), personal communication.

[80] Wang, A.S.D., Barsoum, M.W., and Huang, X.G., "Matrix Cracking Initiation in Brittle-Matrix Composites", *J. Composite Mater.* (1989).

[81] Mason, W.P. and Thurston, R.N., *Physical Acoustics: Principles and Methods*, Vol. 16, New York: Academic Press, (1982).

[82] Rice, R.W., "Perspective on Fractography", in *Fractography of Glasses and Ceramics*: Proc. of Conf. on Fract. of Glasses and Ceramics, eds. J.R. Varner and V.D. Frechette, Alfred University, Alfred, NY, (1986).

[83] Generazio, E.G., NASA Lewis Research Center, Cleveland, OH, (1991), personal communication.

[84] Hertzberg, R.W., *Deformation and Fracture Mechanics of Engineering Materials*, 3rd ed., New York: John Wiley & Sons, Inc., (1989).

[85] Swanson, P.L., "Crack-Interface Traction: A Fracture Resistance Mehcanism in Brittle Polycrystals", in *Fractography of Glasses and Ceramics*: Proc. of Conf. on Fract. of Glassses and Ceramics, eds. J.R. Varner and V.D. Frechette, Alfred University, Alfred, NY, (1986).

[86] Lawn, B., National Institute of Standards and Technology, Gaithersburg, MD, (1992), personal communication.

[87] Marshall, D.B., Rockwell International, Thousand Oaks, CA, (1992), personal communication.

[88] Pletka, B.J. and Wiederhorn, S.M., "Subcritical Crack Growth in Glass-Ceramics", in *Fracture Mechanics of Ceramics: Crack Growth and Microstructure*, eds. R.C. Bradt, D.P.H. Hasselman, and F.F. Lange, vol. 4, New York: Plenum Press, (1978).

[89] Aveston, J. and Kelly, A., "Theory of Multiple Fracture of Fibrous Composites", *J. of Mat. Sci.*, 8, 352-62 (1973).

[90] Broutman, L.J. and Krock, R.H. eds., *Modern Composite Materials*, Reading, MA: Addison-Wesley Publ. Co., (1967).

[91] Cherepanov, G.P., *Mechanics of Brittle Fracture*, trans. A.L. Peabody, New York: McGraw-Hill Book Co., Inc., (1979).

[92] Lynnworth, L.C., *Ultrasonic Measurements for Process Control: Theory, Techniques, Applications*, New York: Academic Press, (1989).

[93] Roth, D.J., "Property and Microstructural Nonuniformity in the Yttrium-Barium-Copper-Oxide Superconductor Determined from Electrical, Magnetic, and Ultrasonic Measurements, Ph.D. Dissertation: Case Western Reserve University, (1991).

[94] Sears, F.W., Zemansky, M.W., Young, H.D., *University Physics*, 6th ed., Reading, MA: Addison-Wesley Publishing Co., (1982).

[95] Vary, A., "NDE Standards for High Temperature Materials", *NASA TM 103761* (1991).

[96] Lemons, R.A. and Quate, C.F., "Acoustic Microscope-Scanning Version", *App. Phys. Lett.*, 24 (4), 163-5, (1974).

[97] Kessler, L.W., "Acoustic Microscopy", *Metals Handbook*, Vol. 17, 9th ed.: Nondestructive Evaluation and Quality Control,

[98] Rohklin, S.I., "Adhesive Joint Evaluation by Ultrasonic Interface and Lamb Waves", in *Materials Analysis by Ultrasonics: Metals, Ceramics and Composites*, ed. A. Vary, Park Ridge, NJ: Noyes Data Corp., (1987).

[99] Vary, A. and Kautz, H.E., "Transfer Function Concept for Ultrasonic Characterization of Material Microstructures", in *Materials Analysis by Ultrasonics: Metals, Ceramics and Composites*, ed. A. Vary, Park Ridge, NJ: Noyes Data Corp., (1987).

[100] Achenbach, J.D., "Flaw Characterization by Ultrasonic Scattering Methods", in *Solid Mechanics Research for Quantitative Non-Destructive Evaluation*, eds. J.D. Achenbach and Y. Rajapakse, Lancaster: Martinus Nijhoff Publ., (1987).

[101] Briggs, G.A.D. and Somekh, M.G., "Acoustic Microscopy of Surface Cracks: Theory and Practice", in *Solid Mechanics Research for Quantitative Non-Destructive Evaluation*, eds. J.D. Achenbach and Y. Rajapakse, Lancaster: Martinus Nijhoff Publ., (1987).

[102] Lucas, R. and Biquard, P., *J. Phys. Rad.*, 3, 464 (1932).

[103] Korpel, A., "Acousto-optics", in *Applied Solid State Science*, Vol. 3: Advances in Materials and Device Research, ed. R. Wolfe, New York: Academic Press, (1972).

[104] Ippen, E.P., "Diffraction of Light by Surface Acoustic Waves", *Proc. IEEE*, 55, 248-9, (1967).

[105] Adler, R., Korpel, and Desmares P., *IEEE Trans. Sonics Ultrason.*, SU-15, 157, (1968).

[106] Born, M. and Wolf, E., *Principles of Optics* 6th ed., New York: Pergamon Press, Inc., (1980).

[107] Kessler, L.W., McGraw, T.E., and Yuhas, D.E., Acoustic Microscopy Application Seminar-Workshop, (1979).

[108] Yariv, H., *Introduction to Optical Electronics*, New York: Holt, Rinehart & Winston, Inc., (1971).

[109] Brewster, D., *Trans. Roy. Soc. Ed.*, 8 (1818).

[110] Salzmann, E. and Weismann, D., "Optical Detection of Rayleigh Waves", 3408-9, (1969).

[111] Korpel, A., Adler, R., Desmares, P., and Watson, W., "A Television Display Using Acoustic Deflection and Modulation of Coherent Light", *Applied Optics*, 5 (10), 1667-75, (1966).

[112] Nye, S.F., *Physical Properties of Crystals*, London: Oxford Press, (1954).

[113] O'Hare, J.M., "Optical Radiation and Matter", EOP 502, University of Dayton, Dayton, OH, (1988).

[114] Kessler, L.W. and Yuhas, D.E., "Principles and Analytical Capabilities of the Scanning Laser Acoustic Microscope (SLAM), *Scanning Electron Microscopy*, Vol. 1, 555-60 (1978).

[115] Gabor, D., "Microscopy by Reconstructed Wavefronts", *Proc. Roy. Soc.*, A197 (454), (1949).

[116] Irwin, G.R., *Handbuch der Physik*, Vol. 6, Berlin: Springer, (1958).

[117] Hubner, H. and Jillek, W., "Sub-Critical Crack Extension and Crack Resistance in Polycrystalline Alumina", *J. Mater. Sci.*, 12, 117-25, (1977).

[118] Steinbrech, R., Knehans R., and Achaawachter, W., "Increase of Crack Resistance During Slow Crack Growth in Al_2O_3 Bend Specimens", *J. Mater. Sci. Lett.*, 1, 327-9, (1982).

[119] Faber, K. and Evans, A.G., "Crack Deflection Processes: I, Theory; II, Experiment", *Acta. Met.*, 31, 565-84, (1983).

[120] Swanson, P., Fairbanks, C.J., Lawn, B.R., Mai, Y.W., and Hockey, B.J., "Crack-Interface Grain Bridging as a Fracture Resistance Mechanism in Ceramics: I. Experimental Study on Alumina", *J. Am. Ceram. Soc.*, 70, 279-89, (1987).

[121] Swanson, P., "Tensile Fracture Resistance Mechanisms in Brittle Polycrystals: An Ultrasonics and In-Situ Microscopy Investigation", *J. Geophys. Res.*, 92, 8015-36, (1987).

[122] Frechette, V.D., "Characteristics of Fracture-Exposed Surfaces", *Proc. Brit. Ceram. Soc.*, 5, 97-106, (1965).

[123] Sommer, E., Formation of Fracture Lances in Glass", *Eng. Frac. Mech.*, 1, 539-46, (1969).

[124] Pollard, D.D., Segall, P., and Delaney, P.T., "Formation and Interpretation of Dilatant Echelon Cracks", *Geol. Soc. Am. Bull.*, 93, 1291-1303, (1982).

[125] Swanson, P.L., "Crack-Interface Traction: A Fracture-Resistance Mechanism in Brittle Polycrystals", in *Fractography of Glasses and Ceramics*: Proc. of Conf. on Fract. of Glasses and Ceramics, eds. J.R. Varner and V.D. Frechette, Alfred University, Alfred, NY, (1986).

APPENDIX A

MODELS FOR MATRIX CRACKING STRESS

Aveston, Cooper, and Kelly Analysis (ACK Model)

From the work of Aveston et al. [43], the stress required to initiate and propagate matrix cracks can be calculated by employing an energy balance analysis. In the composite, the crack can only extend if the work done on the material due to the applied stress exceeds the sum of the strain energy in the matrix, the strain energy in the fibers, and the work done against the frictional stress in pulling the fibers through the matrix. Using this approach, they show that the strain at which the matrix can first crack is given by

$$\epsilon_m^* = \left(\frac{24 \tau \gamma_m E_f V_f^2}{E_c E_m^2 \phi \, V_m} \right)^{\frac{1}{3}} \qquad (10)$$

where τ is the frictional stress between the fiber and the matrix, γ is the surface energy, V is the volume fraction, E is the longitudinal elastic modulus, and ϕ is the diameter of the fiber. The *f, m,* and *c* subscripts denote the fiber, matrix, and composite respectively. Using this expression, the first matrix cracking stress is

$$\sigma_m^* = \epsilon_m^* E_c \qquad (11)$$

While the Aveston analysis is accurate to a first approximation, it has two fundamental limitations for real composite systems. The stresses required for cracking ceramic composites are dependent upon the distribution of the flaw population throughout the material rather than on the existence of a critical flaw as in monolithics. In addition, the Aveston analysis only considers the energies before and after the crack propagation has occurred. A rigorous development would entail an energy analysis of incremental crack extensions. Such a development was completed by Marshall et al. [44].

Marshall, Cox, and Evans Analysis (MCE Model)

The Marshall analysis shows that there is a critical crack extension stress which is a material characteristic of the composite given by

$$\sigma_0 = 6^{\frac{1}{3}} [2 (1-\nu^2) K_{mc}^2 \tau E_f V_f^2 V_m (1+\eta)^2 / E_m \phi]^{\frac{1}{3}} \qquad (12)$$

where ν is the Poisson's ratio, K_{mc} is the critical stress intensity factor for the matrix, and $\eta = E_f V_f / E_m V_m$. Using the properties tabulated for the appropriate fibers and matrices in Chapter IV, the critical matrix cracking stress is calculated to be 265 MPa and 376 MPa for a 50 volume percent LAS/Nicalon SiC and a 40 volume percent CAS/Nicalon SiC fiber reinforced composite, respectively.

It is important to note that equations (10) and (12) are only valid for "long" crack lengths. In this scenario, the critical stress is independent of crack length and is thus a material parameter. Using a fracture mechanics analysis, Marshall et al. show that for "short" cracks, i.e., for a crack length, c, less than $c_m/3$, the stress required to propagate cracks is, in normalized form,

$$\frac{\sigma}{\sigma_m} = \frac{1}{3}\left(\frac{c}{c_m}\right)^{-\frac{1}{2}} + \frac{2}{3}\left(\frac{c}{c_m}\right)^{\frac{1}{4}} \qquad (13)$$

where $\sigma_m = 0.98\sigma_0$ and

$$c_m = \frac{\pi}{4\chi^{4/3}}\left(\frac{K_{mc}E_m V_m^2 \eta \phi (1-\nu^2)}{2\tau V_f^2 E_f}\right)^{\frac{2}{3}} .$$

χ is a dimensionless constant characteristic of the crack geometry. For straight cracks, χ=1.2. Thus, for short cracks, the stress required to propagate matrix cracks decreases as the crack length increases. Beyond the critical crack length, the matrix cracking stress becomes independent of crack size and the material becomes notch insensitive. The critical crack length for the LAS/Nicalon system is calculated from material parameters [33,39] to be 108 μm. Thus, the critical crack length represents approximately 7 fiber diameters in this system.

Consider a uniform homogeneous composite material in four-point flexure as shown in Figure 29. As the composite material is stressed, the matrix deforms locally as previously described. This local deformation gives rise to stress and strain contours in the vicinity of the propagating matrix cracks. Assuming the rule of

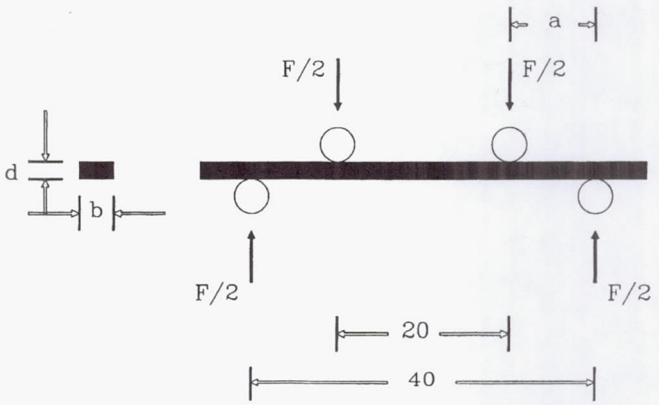

Figure 29.—Four-point flexure configuration.

mixtures model approximation applies, Equation (12) can be used to determine the load at which the material is expected to exhibit its macroscopic "yield" point, i.e., the domination of matrix damage and steady state cracking. For a uniform flexural specimen, this load, in terms of microstructural parameters, is

$$F_y = \frac{4I}{ad}\left(\frac{24\gamma_m \tau E_f V_f^2 E_c^2}{\phi V_m E_m^2}\right)^{\frac{1}{3}} \tag{14}$$

where I is the moment of inertia of the flexural bar. The other parameters are as previously defined or identified in the figure. Once this load is reached, the tensile surface of the flexural specimen becomes extensively cracked and the load is not effectively transferred to the fibers. Therefore, a large part of the fibers do not contribute to the stiffness of the system.

The cumulative damage in the matrix diminishes the uniformity of the stress distribution in the composite if stresses are applied subsequent to initial matrix

cracking. In this case, the apparent stresses on the specimen may differ considerably from the actual applied stresses and linear elastic beam theory is no longer necessarily applicable to the flexure system.

APPENDIX B

THEORY OF SLAM OPERATION

An acoustic wave propagating through a material fundamentally causes a perturbation of the microscopic structural arrangement in the material. Assume that the acoustic wave propagates through an ideal defect-free isotropic media. The relative microscopic perturbation caused by the propagating wave strains the material locally and leads to a redistribution of the localized density profiles within the material as shown in Figure 30. In a nonideal media, the velocity of the sound propagation is altered in the vicinity of any elastic inhomogeneities and the acoustic phase front is

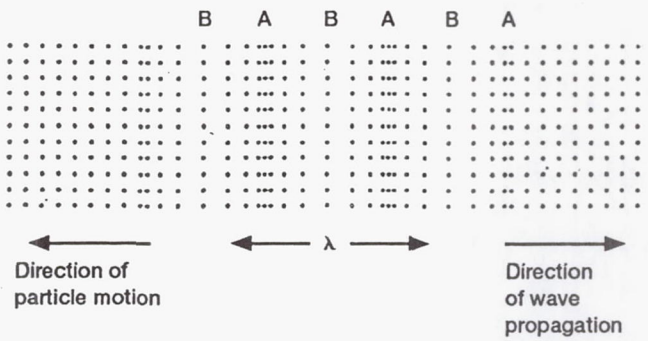

Figure 30.—Propagation of acoustic waves.

altered by diffraction. The resulting diffraction patterns can be used to analyze the internal structural arrangement of a material specimen. This is the principle used in acoustic microscopy to locate and characterize defects in monolithic materials and debonding in composite materials [96-101].

In the scanning laser acoustic microscope, a specimen is insonified with a high frequency ultrasonic (acoustic) wave. The acoustic strain produced is detected by means of a scanning helium neon (HeNe) laser beam. The acousto-optical response is converted to an electrical signal at a photodetector. There is an acoustically induced temporal and spatial phase modulation of the optical wave. This interaction between the optical pulse and the acoustic wave may be described and modelled by [30]

1. A periodic phase modulation which is a direct function of the normal surface displacement caused by the acoustic wave disturbance (often referred to as dynamic ripple in the literature)
2. A periodic deflection related to the slope of the surface displacement
3. A periodic focusing and defocusing of the surface related to the curvature of the surface displacement
4. A temporally and/or spatially periodic phase corrugation which replicates the acoustic displacement pattern.

Much of the previous literature regarding the SLAM system configuration and application thereof employs models incorporating the effect of the acoustic perturbation on the tilting of the corrugated surface as a method of relating the optical response to acoustic field parameters [26,30,102]. This model shows that the power received at the photodetector is [30]

$$P = P_0\left(\frac{f}{D}\right)\left(\frac{4\pi}{\Lambda}\right)\Gamma\cos(\omega_m t + \psi) \qquad (15)$$

where P_0 is the total power of the projected optical response at the detector, f is the focal length of the focusing lens, D is the diameter of the lens aperture, Λ is the acoustic wavelength along the surface of the specimen, Γ is the peak amplitude of the surface corrugation due to the propagating acoustic wave, ω_m is the frequency of the propagating surface wave, t represents time, and ψ is the phase of the signal. The use of this model for quantitative analysis of the specimen material would require quantitative information about the acoustic field parameters such as the amplitude of the surface wave. These parameters are difficult to experimentally assess, making this model of little value for quantitative analyses.

The interaction between the optical and acoustic waves can also be regarded as a diffraction phenomena [30,103-105]. In this case, the corrugated surface acts as an optical grating to the incident coherent beam and the optical response is to diffract the image into several orders. From diffraction theory, the first two orders

are located at $\pm\lambda/\Lambda$ with respect to the zero order [106]. In this model, the diffracted signal is Doppler frequency shifted by an amount ω_m, the magnitude of the acoustic frequency at the specimen surface [30].

The character of the detected optical signal is strongly dependent upon the interaction length between the acoustic and optical waves. If the transverse dimensions of the acoustic wave are small and the interaction length is short, multiple orders of diffraction are observed. This corresponds to the case

$$s >> \Lambda \tag{16}$$

where s is the diameter of the laser spot at the region of interest and Λ corresponds to the wavelength of the acoustic wave in the specimen.

If the transverse dimensions of the acoustic wave are large and the interaction length is long, a single order of diffraction is observed. This is the case when

$$s < \Lambda. \tag{17}$$

In the existing SLAM system, $s = \frac{1}{2}\Lambda$ so this diffraction response is operable [107]. The incident laser beam is phase shifted by an amount corresponding to the particular acoustic wave propagation vector [108].

The surface is affected by the bulk acousto-optical properties of the material. The acoustic strain modulates the index of refraction of the material. This phenomena is described as the photoelastic effect [109]. A rigorous treatment of

acoustic waves propagating along the surface of a specimen would include the effects of both the surface corrugation and the modulation of the index of refraction. However, researchers have experimentally shown that the effect of surface corrugation is negligible in relationship to the modulation of the refractive index for a given specimen [110]. In addition, the bulk affects the surface modulation; the amplitude of the surface wave propagation is proportional to the index of refraction modulation [111]. Therefore, it is legitimate to analyze the acousto-optical signal response by considering either the effect of the surface corrugation or the index modulation.

Mathematically, the magnitude of the modulation is described, in contracted notation, by a deformation of the optical indicatrix of the material as [112,113]

$$\Delta B_j = p_{jk} \epsilon'_k \tag{18}$$

where ΔB_j represents the change in the relative dielectric impermeability tensor, p_{jk} is the strain-optic coefficient determined by the crystal class symmetry of the material, and ϵ'_k is the strain induced by the acoustic wave. This formulation assumes that the strains produced in the material are elastic and that there is a negligible rotation component to the strain. The acoustic strain is sinusoidal resulting in a modulation of the index of refraction in the material given by

$$\Delta n_j = \frac{-n_0^3}{2} \Delta B_j \tag{19}$$

where n_0 is the index of refraction along the principal axes. Effectively, a measurable phase modulation of a coherent laser beam which interacts with the acoustic wave is induced.

In the SLAM system, the phase modulation of the reflected laser light is detected as an angular modulation of the received wave. The region of interest is laser-scanned point by point; at each point the angular modulation is updated. A knife edge is placed in the path of the received light wave. This converts the angular light modulation to an intensity modulation which can be viewed on an image monitor [114]. Each image contains information from 40000 points within the field of view.

The phase modulated optical wave at the detector is superposed with an electronic phase reference signal. These superposed signals interfere to form a series of fringes whose spacing and orientation is characteristic of the internal structure at the region of interest on the specimen. The fringes formed are similar in principle to those formed in holographic imagery [115].

The velocity of sound in a material can be measured using the interference option of the SLAM. According to Snell's law, there is a definitive acoustic refraction relationship at the interface between two acoustic boundaries. This is described by

$$\frac{\sin\theta_0}{v_0} = \frac{\sin\theta_x}{v_x} \qquad \textbf{(20)}$$

where v_0 and v_x represent the velocity of sound in the surrounding media and the

specimen, respectively. If the thickness of the specimen is given by d, the detected interference fringe shift, normalized by the unperturbed spacing of the fringes, is[107]

$$N = \frac{d \sin\theta_0}{\Lambda_0} \left(\frac{1}{\tan\theta_0} - \frac{1}{\tan\theta_x} \right). \qquad (21)$$

Combining equations (20) and (21) yields an equation to experimentally determine the velocity of sound in the material. This fringe shift is a measure of the normalized phase shift of the acoustic wave as the state of stress of the material changes. As previously described, the phase shift is a direct function of the modulation of the refractive index within the material.

APPENDIX C

MODEL FOR MEASURING STRAIN IN SLAM

Damage accumulation within a specimen is expected to give rise to a localized strain distribution in the vicinity of the specimen damage. As the strain distribution changes, the index modulation within the material changes accordingly. The updated modulation will be indicated by a fringe shift in the SLAM interferogram.

The relationship between the internal strain in the system and the magnitude of the fringe shift is found by determining the difference in the acousto-optic path length between the two stress states of interest. As strain accumulates in the matrix, the acousto-optic path difference between the stress states of interest changes due to a macroscopic change in the length of the stressed region and due to alterations of the index modulation as described by equation (19). The incremental acousto-optic path difference is given by

$$\Delta\delta = l\Delta n + n\Delta l \qquad (22)$$

where n is the index of refraction in the material, l is the length of the stressed region, and Δ represents incremental changes in each of these parameters due to the

internal strains. Using equations (18), (19), and (22), the acousto-optic path difference at the initial stress state may be written

$$(\delta_j)_{init} = -\frac{n_0^3}{2} l p_{jk} \epsilon_k' \tag{23}$$

where we have used the fact that the incremental change in length is zero at the initial stress state.

When an external stress is applied to the material, the resulting internal strain alters the modulation of the refractive index and the acoustic difference changes. If the load is applied along the x_1 direction, the deformation of the optical indicatrix is represented by

$$\begin{pmatrix} \Delta n_1 \\ \Delta n_2 \\ \Delta n_3 \\ \Delta n_4 \\ \Delta n_5 \\ \Delta n_6 \end{pmatrix} = \frac{-n_0^3}{2} p_{jk} \begin{pmatrix} \epsilon_1' + \epsilon_1 \\ \epsilon_2 \\ \epsilon_3' + \epsilon_3 \\ \epsilon_4 \\ \epsilon_5 \\ \epsilon_6 \end{pmatrix} \tag{24}$$

where the primed strains refer to those induced by the propagating acoustic field and the unprimed strains result from the application of the mechanical stress. For the purpose of this study, we assume that the specimen is in pure flexure and that the region of interest contains no shear strains. These conditions simplify equation (24) since $\epsilon_4 = \epsilon_5 = \epsilon_6 = 0$. Using this equation, the incremental acousto-optic path

difference is given by

$$(\delta_j)_{fin} = n_0 \Delta l_j - \frac{n_0^3}{3} l p_{jk} (\epsilon_k' + \epsilon_k) \tag{25}$$

The total acousto-optic path difference at the initial and final states respectively is found by integrating the appropriate incremental path difference over the total path length as

$$\Delta_j = \int_s \delta_j \, ds \tag{26}$$

The magnitude of the interferometric phase shift is related to the difference in total path lengths between the initial and final states. When the appropriate integrations and subtractions are performed, the total path difference is determined

$$\Delta(\Delta_j) = l(n_0 \epsilon_j - \frac{n_0^3}{2} p_{jk} \epsilon_k) \tag{27}$$

The total path difference contains information from each of the normal strains. However, by using the fact that the normal strains are related to each other by Poisson's ratio and considering the path difference in only the x_1 direction, a functional relationship between the strain and the fringe displacement is determined. This is given by

$$\epsilon_1 = \frac{m\Lambda}{l\left(n_0 - \frac{n_0^3}{2}\xi_1\right)} \tag{28}$$

where m is an integral number and

$$\xi_1 \doteq p_{11} + \nu_{21} p_{12} + \nu_{31} p_{13}. \tag{29}$$

The system measurement accuracy in the interference mode is directly a function of the accuracy with which the interference fringe shift can be measured. In the interference mode, it has been shown in previous work that 1% changes in the velocity of sound through the medium produce discernible shifts in the interference fringe field [107].

APPENDIX D

DESIGNS FOR FLEXURAL FIXTURE

The following flexural fixture design is drawn to scale. All dimensions are given in inches unless otherwise noted. A photograph of the fixture showing the placement of the load cell and specimen is given on the following page.

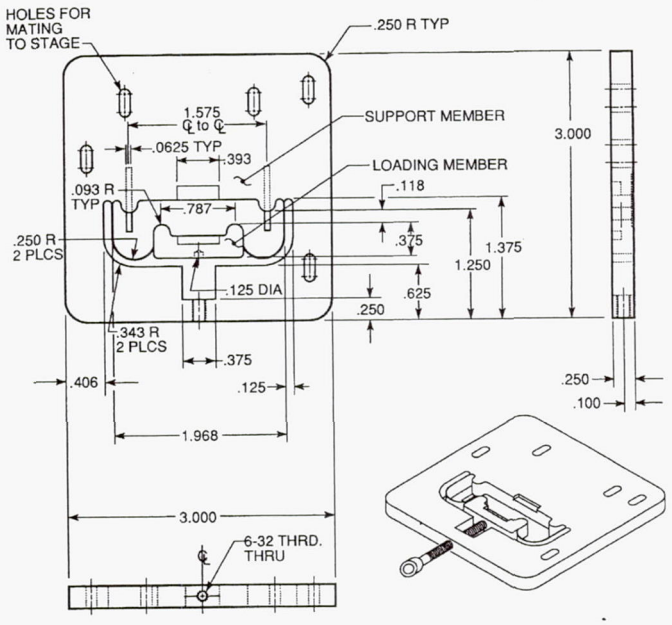

Appendix D.

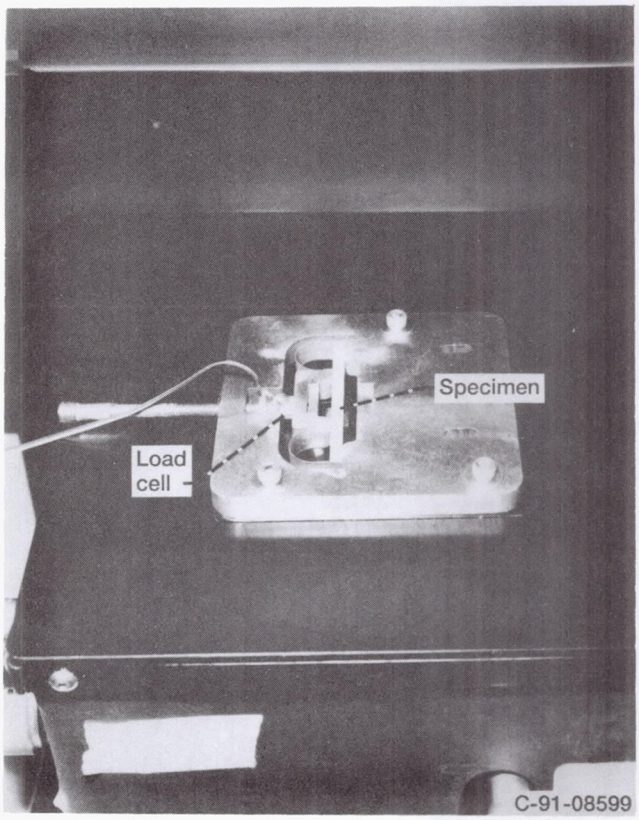

Figure 31.—Flexural fixture used in SLAM.

APPENDIX E

TENSILE STRAIN MEASUREMENTS FOR NICALON SiC FIBER

Table 9: Experimental SLAM Strain Data for Nicalon SiC Fibers Specimens 1-15

		Strain (ϵ), (x 10^{-3})		
Fiber	**Diameter (μm)**	**Load A (10 g)**	**Load B (15 g)**	**Load C (20 g)**
1	17.50	2.17	3.36	4.63
2	15.95	3.59	5.23	7.32
3	16.25	2.61	3.88	5.23
4	13.64	3.73	5.68	6.26
5	14.62	4.11	5.68	7.99
6	14.23	3.21	4.11	6.20
7	15.43	3.66	5.53	7.55
8	15.37	2.99	4.03	5.23
9	14.62	3.21	4.41	6.13
10	15.00	3.14	4.71	6.72
11	14.44	2.84	4.30	5.75
12	14.52	4.03	6.13	8.07
13	15.82	3.06	4.33	5.38
14	13.64	4.11	5.30	7.69
15	14.00	3.44	5.08	6.87

APPENDIX F

STRAIN MEASUREMENTS FOR LITHIUM ALUMINO-SILICATE (LAS)

Table 10: Experimental SLAM Strain and Residual Strain Data for LAS Specimens 1-5

Stress (MPa)	**Strain (ϵ), (x 10^{-3})**				
	#1	#2	#3	#4	#5
22	1.85	1.95	2.47	2.67	3.14
31	2.30	3.20	3.51	4.00	3.40
41	2.71	4.63	6.53	5.43	4.49
55	4.58	5.77	7.03	8.11	5.50
61	8.71	7.93	7.66	9.23	6.06
67	9.36	9.30	9.61	11.00	7.30
74	9.93	9.65	10.49	11.67	8.76
ϵ_r	2.38	1.99	2.47	2.67	2.30

Table 11: Experimental SLAM Strain and Residual Strain for LAS Specimens 6-9

Stress (MPa)	**Strain (ϵ), (X 10^{-3})**			
	#6	#7	#8	#9
22	3.43	2.61		2.01
31	4.69	3.70	3.70	3.67
41	6.26	5.84	5.91	5.79
55	8.49	7.52	8.60	
61	9.50	8.98	11.65	
67	10.50	9.54	14.01	
74	12.40	11.20	17.72	
ϵ_r	3.00	2.36	4.31	1.75

APPENDIX G

MICROSTRUCTURAL EFFECT ON FRACTURE BEHAVIOR

The fracture behavior of brittle polycrystalline materials has been widely accepted to be based upon the Griffith flaw theory [1]. Simply put, Griffith stated and experimentally verified that the strength of amorphous materials was limited by the size and presence of existing flaws and flaw populations in the material. This concept gave rise to the damage tolerant criteria for design of brittle polycrystals based on fracture mechanics [116]. Basically, this design philosophy maintains that a given component contains inherent flaws which limit its strength and load bearing capability. The component is then designed to experience stress levels below this critical limit.

However, the mechanical properties of a material are crack length dependent, implying a microstructural element associated with fracture. In effect, the mechanical behavior is altered at the microstructural level due to factors contributing to the net crack driving force [29]. In this case, steady state cracking does not necessarily dominate the material. If the crack or microcrack in the material is small in comparison with the grain size, the propagation of the crack and evolution of fracture

is actually influenced and, in many cases, resisted by the presence of the microstructure [117,118].

Several mechanisms accounting for the resistance to fracture in single-phase nontransforming ceramics at the microstructural level have been proposed [88,119]. These mechanisms include frontal-zone microcracking, frictional interlocking of rough fracture surfaces, and ligamentary bridging of debris left behind by the advancing crack front.

The models contend that brittle polycrystalline materials can be likened to fiber reinforced composite materials, in terms of their micromechanical response to fracture. As the crack front propagates through the material, restraining forces shield the primary crack tip from high stress levels. If this restraining field is not overcome, the primary crack will either deflect or suspend propagation.

At the microstructural level, the fracture phenomenon and associated stress field is a function of the position of the crack. As the crack encounters microstructural anomalies, such as variations in grain orientation or elastic inhomogeneities, the crack tip is deflected or impeded. In the frontal zone cracking model, a diffuse microcrack region is formed at the location of the crack-microstructure interaction. In this region, distributed microcracking and secondary cracking is observed [119]. Secondary cracking can often also occur behind the primary crack tip [120,121].

The ligamentary bridging model is an extension of mechanisms used to explain fracture behavior of simple materials such as glasses [122,123,124]. In this model, the initial fracture encounters an altered stress state at the microstructural anomaly and splits into several parallel secondary cracks. Individual grains in crystalline ceramics and/or debris left by the primary crack join the array of secondary cracks and act to resist continued propagation. The presence of ligamentary bridging has been experimentally observed in glasses [122], fine-grained alumina [125], and glass ceramics [125].

In the fine-grained glass ceramics, local inhomogeneities in the microstructure combined to form larger bridges. Large size ligaments also formed in glass ceramics subjected to incremental loading to subcritical load levels. As the crack encounters variations in grain orientation, it experiences subtle differences in the applied stress level. This gives rise to alterations in the traction at the local crack-interface and local segmentation of the crack may occur.

A key element to understanding the mechanical behavior of a material is to correlate the effect the crack-microstructure interaction with the macrocrack and observed macromechanical behavior. If the micromechanical interaction dominates the fracture behavior, the macrocrack may be influenced and experience similiar crack deflection phenomena. This effect is prevalent in fiber reinforced composite materials. If the micromechanical interaction is essentially a stochastic process, the

behavior is likely to be normalized at the macromechanical level and the individual micromechanical elements would not typically be observed. This behavior is typical in monolithic ceramic materials.

APPENDIX H

STRAIN MEASUREMENTS FOR LAS/SiC MONOFILAMENT COMPOSITE

Table 12: Experimental SLAM Strain and Residual Strain Data for LAS/SiC Specimens 1-5

Stress (MPa)	**Strain (ϵ), (x 10^{-3})**				
	#1	#2	#3	#4	#5
22	3.52	2.98	4.98	3.93	1.50
31	6.31	13.47	8.49	9.50	2.09
41	7.32	17.07	12.22	12.73	5.10
56	11.09	20.66	28.74	12.96	6.89
61	14.12	32.56	33.68	24.70	9.88
67	17.40	N/A	34.81	26.05	11.38
74	20.19	34.13	39.75	26.72	18.26
ϵ_r	5.05	2.09	2.49	5.79	4.49

Table 13: Experimental SLAM Strain and Residual Strain Data for LAS/SiC Specimens 6-10

Stress (MPa)	**Strain (ϵ), (x 10^{-3})**				
	#6	#7	#8	#9	#10
22	3.48	7.30	3.79	2.83	3.05
31	5.66	9.32	5.50	3.70	3.55
41	12.19	11.95	7.30	5.96	6.13
56	15.47	16.03	21.38	8.51	10.15
61	17.22	18.08	31.44	11.99	12.06
67	22.32	23.58	36.83	N/A	13.94
74	25.15	26.50		15.27	15.83
ϵ_r	5.88	12.82	4.00	4.36	3.77

APPENDIX I

STRAIN MEASUREMENTS FOR CAS/SiC COMPOSITES

Table 14: Experimental SLAM Strain and Residual Strain Data for CAS/SiC Specimens 1-4.

Stress (MPa)	Strain (ϵ), (x 10^{-3})			
	#1	#2	#3	#4
15	0.556	0.447	0.334	0.334
26	0.667	0.574	0.834	0.834
38	1.11	0.761	1.00	1.00
49	1.33	0.995	1.27	1.50
63	1.67	1.14	1.99	1.67
76	2.22	1.93	2.50	2.50
ϵ_r	1.33	0.995	1.67	1.50

REPORT DOCUMENTATION PAGE

Form Approved
OMB No. 0704-0188

1. AGENCY USE ONLY (*Leave blank*)	2. REPORT DATE	3. REPORT TYPE AND DATES COVERED
	March 1993	Final Contractor Report

4. TITLE AND SUBTITLE
Internal Strain Analysis of Ceramics Using Scanning Laser Acoustic Microscopy

5. FUNDING NUMBERS
WU–510–01–50
NCC3–81

6. AUTHOR(S)
Renee M. Kent

7. PERFORMING ORGANIZATION NAME(S) AND ADDRESS(ES)
University of Dayton
Dayton, Ohio 45469

8. PERFORMING ORGANIZATION REPORT NUMBER
E–7308

9. SPONSORING/MONITORING AGENCY NAMES(S) AND ADDRESS(ES)
National Aeronautics and Space Administration
Washington, D.C. 20546–0001

10. SPONSORING/MONITORING AGENCY REPORT NUMBER
NASA CR–191118

11. SUPPLEMENTARY NOTES
Renee M. Kent, University of Dayton, Dayton, Ohio 45469 and NASA Resident Research Associate at Lewis Research Center. Project Manager, Alex Vary, Structures Division, NASA Lewis Research Center, (216) 433–6019.

12a. DISTRIBUTION/AVAILABILITY STATEMENT
Unclassified - Unlimited
Subject Category 38

12b. DISTRIBUTION CODE

13. ABSTRACT ***(Maximum 200 words)***

Quantitative studies of material behavior characteristics are essential for predicting the functionality of a material under its operating conditions. A nonintrusive methodology for measuring the in situ strain of small diameter (to 11 μm) ceramic fibers under uniaxial tensile loading and the local internal strains of ceramics and ceramic composites under flexural loading is introduced. The strain measurements and experimentally observed mechanical behavior are analyzed in terms of the microstructural development and fracture behavior of each test specimen evaluated. Measurement and analysis of Nicalon silicon carbide (SiC) fiber (15 μm diameter) indicate that the mean elastic modulus of the individual fiber is 185.3 GPa. Deviations observed in the experimentally determined elastic modulus values between specimens were attributed to microstructural variations which occur during processing. Corresponding variations in the fracture surface morphology were also observed. The observed local mechanical behavior of a lithium alumino-silicate (LAS) glass ceramic, a LAS/SiC monofilament composite, and a calcium alumino-silicate (CAS)/SiC fully reinforced composite exhibits nonlinearities and apparent hysteresis due to the subcritical mechanical loading. Local hysteresis in the LAS matrices coincided with the occurrence of multiple fracture initiation sites, localized microcracking and secondary cracking. The observed microcracking phenomenon was attributed to stress relaxation of residual stresses developed during processing, and local interaction of the crack front with the microstructure. The relaxation strain and stress predicated on apparent mechanical hysteresis effects were defined and correlated with the magnitude of the measured fracture stress for each specimen studied. This quantitative correlation indicated a repeatable measure of the stress at which matrix microcracking occurred for stress relief of each material system. Stress relaxation occurred prior to the onset of steady state cracking conditions. The relaxation stress occurred at 18.5 percent of the fracture stress in LAS and 11.0 percent of the yield stress in CAS/SiC. The relaxation stress ratio was dependent upon the dominant fracture mode of the LAS/SiC specimens. Relaxation stress ratios greater than 0.30 were observed for specimens which fractured due to shear at the fiber matrix interface; specimens which fracture due to tensile cracking had relaxation stress ratios less than 0.30. The stress relaxation ratio appeared to be a specific characteristic of the glass ceramic material. The measured stress relaxation for LAS indicated a measure of the inherent residual stresses in the material due to processing and suggested localized toughening mechanisms for brittle material structures.

14. SUBJECT TERMS	15. NUMBER OF PAGES
Strain; Ceramic; Fiber; Ceramic matrix composite; Nonintrusive	134
	16. PRICE CODE A07

17. SECURITY CLASSIFICATION OF REPORT	18. SECURITY CLASSIFICATION OF THIS PAGE	19. SECURITY CLASSIFICATION OF ABSTRACT	20. LIMITATION OF ABSTRACT
Unclassified	Unclassified	Unclassified	